Science for Energy and Environment
https://www.sciltp.com/journals/see

Review

Electrochemical N_2 Conversion: Reduction and Oxidation Pathways under Mild Conditions

Xingyu Ma [1], Xuanhe Wang [2,3], Jingwen Liu [2,3] and Yibo Ma [2,3,*]

[1] School of Chemical Engineering, University of Science and Technology Liaoning, Anshan 114051, China
[2] Centre for Atomaterials and Nanomanufacturing (CAN), School of Science, RMIT University, Melbourne, VIC 3000, Australia
[3] ARC Industrial Transformation Research Hub for Intelligent Energy Efficiency in Future Protected Cropping (E2Crop), Melbourne, VIC 3000, Australia
* Correspondence: yibo.ma@rmit.edu.au

How To Cite: Ma, X.; Wang, X.; Liu, J.; et al. Electrochemical N_2 Conversion: Reduction and Oxidation Pathways under Mild Conditions. *Science for Energy and Environment* **2026**, *3*(1), 1. https://doi.org/10.53941/see.2026.100001

Received: 10 December 2025
Revised: 1 January 2026
Accepted: 5 February 2026
Published: 2 March 2026

Abstract: Electrochemical nitrogen fixation (EN_2F) is emerging as a promising technology. This review summarizes recent advances in both nitrogen reduction reaction (N_2RR) and nitrogen oxidation reaction (N_2OR) pathways for ammonia synthesis under mild conditions. We begin by contrasting the fundamental reactions and mechanisms of N_2RR and N_2OR, emphasizing the impact of competing hydrogen evolution reaction (HER) and oxygen evolution reaction (OER) on EN_2F selectivity. A detailed analysis of various N_2RR mechanisms, including dissociative, associative, Mars-van Krevelen, surface-hydrogenation, and dual-site pathways, is presented, highlighting their respective advantages and limitations. For N_2OR, we focus on O-preferred and N-preferred reaction routes, emphasizing the role of hydroxyl species in N_2 activation. Progress in catalyst development for both N_2RR and N_2OR is summarized, with particular attention to surface-hydrogenation or dual-site mechanisms, as well as strong/weak N-bonding bimetallic catalysts. Strategies for promoting N_2OR by modulating the OER are also discussed. Furthermore, we analyze the kinetic steps of EN_2F, identifying nitrogen dissolution and mass transfer as potential rate-limiting factors, and propose strategies for enhancing EN_2F selectivity through electrolyte optimization, electrolyzer design, and catalyst modification. Finally, we offer a perspective on the future directions of EN_2F, acknowledging the current challenges of active nitrogen pollution and suggesting avenues for technological advancement through refined experimental protocols, innovative catalyst design, and thermochemical analysis.

Keywords: electrochemical nitrogen fixation; nitrogen reduction; nitrogen oxidation; catalyst mechanisms; selectivity

1. Introduction

It is essential to increase agricultural productivity and sustainable food production to reduce the risk of hunger. Approximately 80% of industrial ammonia is consumed as fertilizer [1,2], and increasing its production will contribute to alleviating hunger and overcoming the global epidemic [3,4]. Ammonia is a crucial chemical, serving as a carbon-free fuel and a readily transportable hydrogen carrier [5–7]. Furthermore, nitric acid, derived from ammonia, is a fundamental raw material in the chemical industry, with significant applications as an explosive and in the pharmaceutical and chemical fiber sectors [8,9].

Currently, the Haber-Bosch (HB) process is employed to produce ammonia from fossil fuels, followed by the Oswald process to convert ammonia into nitric acid. Both processes necessitate high temperature

and pressure, demanding substantial energy input. Their combined simplified flow is depicted in Figure 1. The HB process generates H_2 via steam reforming (1); and water-gas shift (2); reactions, consuming 1–2% of global energy and contributing over 1.44% of CO_2 emissions [10,11]. In the ammonia synthesis reactor, N_2 and H_2 react under extreme conditions (3); requiring continuous circulation to improve the conversion rate, each of which is only 15% [12,13]. The subsequent ammonia oxidation reaction (4); under similarly stringent conditions produces NO, which is a major industrial source of the greenhouse gas N_2O. NO is then oxidized (5); and absorbed (6) to yield nitric acid. While the latter two reactions are spontaneous, the overall industrial process is energy-intensive and hazardous [8,14].

Haber-Bosch process:

$$CH_4 + H_2O = CO + 3H_2 \quad (1)$$

$$CO + H_2O = CO_2 + H_2 \quad (2)$$

$$N_2 + 3H_2 = 2NH_3 \quad (3)$$

Ostwald process:

$$4NH_3 + 5O_2 = 4NO + 6H_2O \quad (4)$$

$$2NO + O_2 = 2NO_2 \quad (5)$$

$$3NO_2 + H_2O = 2HNO_3 + NO \quad (6)$$

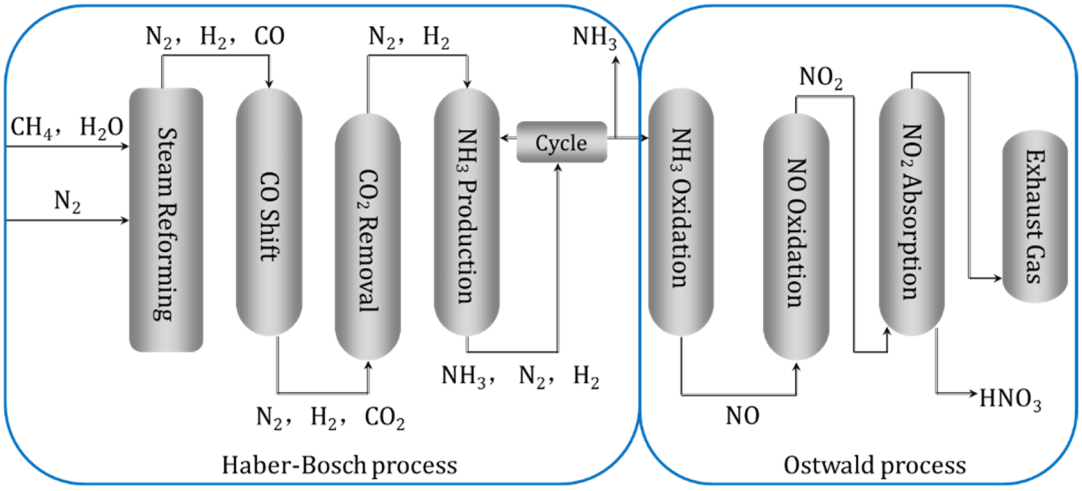

Figure 1. Simple process flow of the combination of Haber-Bosch process and Ostwald process.

With the growing prevalence of intermittent renewable power sources, the electrification and decarbonization of the chemical industry are gaining prominence [15]. Electrochemical nitrogen fixation (EN_2F), powered by renewable energy, is emerging as a third-generation technology expected to increase its market share by 2040 [16]. This approach bypasses the costly steam reforming step and the use of non-renewable resources, while also avoiding the extreme reaction conditions of conventional ammonia production and oxidation. EN_2F utilizes ubiquitous H_2O and N_2 as feedstocks without generating greenhouse gases. Crucially, EN_2F can be implemented on a small, distributed scale, catering to diverse regional needs and mitigating risks associated with centralized nitrogen production [17–20]. Numerous studies have recently investigated electrochemical nitrogen reduction reactions (N_2RR) for ammonia synthesis [21–24]. An alternative route (Figure 2) involves electrochemically oxidizing N_2 to active NO or NO_3^- via N_2OR [25], followed by the reduction of nitric oxide [26,27] or nitrate [28–30] to ammonia. Consequently, EN_2F encompasses two primary technical pathways: N_2RR and N_2OR.

This review aims to integrate the relationship between N_2RR and N_2OR, proposing that EN_2F shares commonalities in nitrogen dissolution, mass transfer, adsorption, activation, competitive reactions, mechanisms, and experimental benchmarking. The first section (Sections 2 and 3) details recent reaction mechanisms and advanced catalysts, highlighting how unavoidable side reactions can influence the activity of main reactions. The second section (Sections 4 and 5) systematically outlines kinetic steps, identifying

nitrogen dissolution and diffusion as potential rate-limiting steps for EN_2F, and discusses selectivity challenges and strategies. Finally, Sections6 presents the prospects and summary of EN_2F, acknowledging the current challenge of active nitrogen pollution while anticipating future applications. The logical structure of the two crossovers is adopted, with the aim of inspiring each other for N_2 fixation.

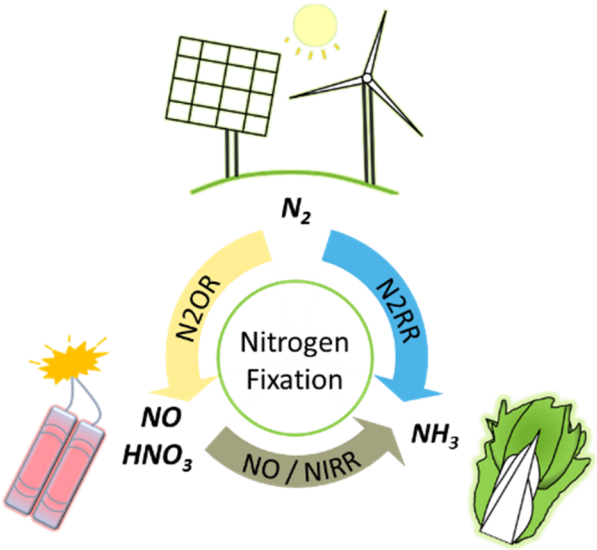

Figure 2. Different routes of NH_3 synthesis from N_2.

2. Basic Reactions and Mechanisms

Theoretically, N_2 fixation can be achieved at atmospheric pressure and temperature using water as the reducing or oxidizing agent and electrons as the driving force [31,32]. The Pourbaix diagram (Figure 3) for the N_2-H_2O system [18] indicates that both N_2RR and N_2OR are pH-sensitive and thermodynamically feasible. However, each faces competition from water electrolysis reactions: hydrogen evolution reaction (HER) for N_2RR and oxygen evolution reaction (OER) for N_2OR. The potential window for N_2RR overlaps with HER across all pH ranges [33], while N_2OR has a narrower overlap with OER at pH > 1.3 [34]. The minimum voltage window for these two reactions (1.08 V) is less than that for water electrolysis (1.23 V) when operating as a full battery. In principle, EN_2F can proceed without side reactions by carefully selecting the operating voltage and electrolytic system (electrolyte, reactor, and catalyst) [18]. Nevertheless, research consistently reveals the occurrence of side reactions, leading to low yields of target products and poor Faradaic efficiencies (FE).

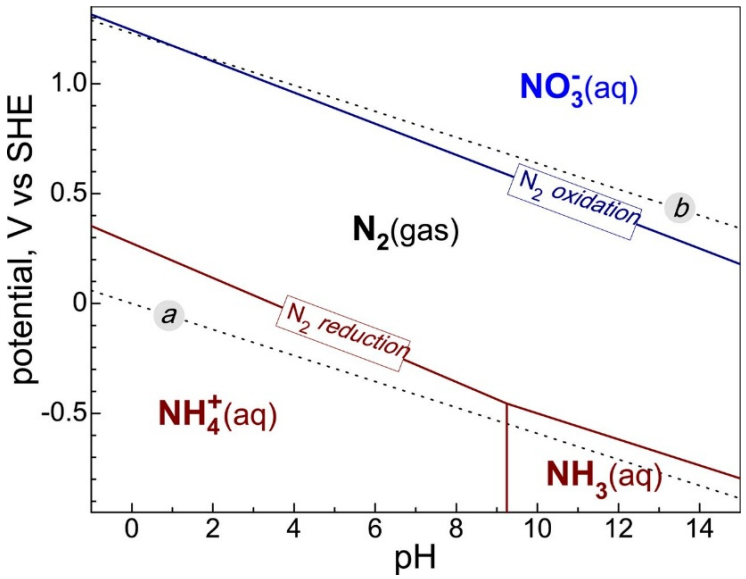

Figure 3. Partial Pourbaix diagram for the N_2-H_2O system. Reprinted with permission from Ref. [18]. Copyright © 2018, The American Association for the Advancement of Science.

2.1. The Relationship between N_2RR and HER

The availability of an active site in N_2RR can be occupied by either N_2 or H. If H^+ and e^- are present and the binding energy of H to the active site is superior to that of N_2, H will adsorb preferentially, leading to the HER side reaction. Conversely, if H^+ transport is inhibited, or if N_2 has a stronger binding energy than H, N_2 will adsorb preferentially. Subsequently, H^+ and e^- can approach and attack or activate the adsorbed N_2 molecule. The cathodic reaction equations for N_2RR and HER are as follows:

Under acidic conditions:

$$N_2RR: N_2 + 6H^+ + 6e^- = 2NH_3 \quad (7)$$

$$HER: 2H^+ + 2e^- = H_2 \quad (8)$$

Under alkaline conditions:

$$N_2RR: N_2 + 6H_2O + 6e^- = 2NH_3 + 6OH^- \quad (9)$$

$$HER: 2H_2O + 2e^- = H_2 + 2OH^- \quad (10)$$

Electrochemical tests show that as the negative voltage increases, ammonia yield and efficiency decrease while hydrogen production increases, indicating that HER becomes dominant. The Pourbaix diagram also suggests that N_2 activation requires operation within a specific optimum potential range, as high negative potentials favor HER and reduce the number of available active sites. Furthermore, N_2RR involves a six-step proton-electron coupling transfer (PECT) with multiple intermediates, whereas HER involves only two steps, kinetically retarding N_2RR [35]. Importantly, the proton source for N_2RR originates from HER, which cannot be entirely suppressed, as this would hinder the hydrogenation of the active site (∗N) [36]. Novel reaction mechanisms and advanced catalysts are discussed further below.

2.2. Mechanisms of N_2RR

Due to the challenge of N_2 activation, different catalytic systems exhibit distinct mechanisms. Reaction pathways are often elucidated by comparing the detailed formation energies of intermediates using density functional theory (DFT) [37,38]. While the HB process has been extensively studied as a benchmark, its detailed mechanism remains debated, particularly concerning whether adsorbed nitrogen is molecular or atomic and whether NH_3 is formed via a dissociative or associative pathway [39]. The following provides an overview of the state-of-the-art N_2RR mechanisms.

2.2.1. Dissociative Mechanism

It is widely accepted that breaking the N_2 triple bond requires harsh conditions of high temperature and pressure. Most studies on industrial catalysts assume a dissociative mechanism (Figure 4A) [39]. In this model, the N≡N triple bond is directly cleaved and adsorbed onto the catalyst surface, which is the rate-determining step (RDS). NH_3 is then formed through sequential protonation of the adsorbed nitrogen atom [40].

The RDS model does not explicitly account for the catalyst's role [41], and the effectiveness of catalysts near the peak of the activity heat map remains unconfirmed. Moreover, many studies on industrial catalysts overlook H_2 dissociation, assuming high ∗N coverage. However, under real steady-state conditions, ∗N and ∗NH coverage is low, influenced by partial pressure [42]. Thus, the steady-state (SS) model (Figure 4B) was introduced to consider environmental effects. In this model, N_2 and H_2 dissociate separately and adsorb onto distinct, proximal active sites. The resulting surface ∗H and ∗N atoms then recombine to form NH_3 [43,44]. The SS model does not predefine an RDS; instead, candidate catalysts are materials that can stably exist under ammonia synthesis conditions and release active hydrogen [40].

Hosono's group has conducted extensive research on catalytic ammonia synthesis under mild conditions [41,44–55], focusing on the electron carrier $C_{12}A_7$:e^- [45]. They proposed a mechanism involving reversible hydrogen storage and release, consistent with the SS model. Here, the RDS shifts from N_2 dissociation to the protonation of ∗N, with Ru/$C_{12}A_7$ catalysts significantly reducing the reaction's activation energy (Figure 5A,B) [41,46,47].

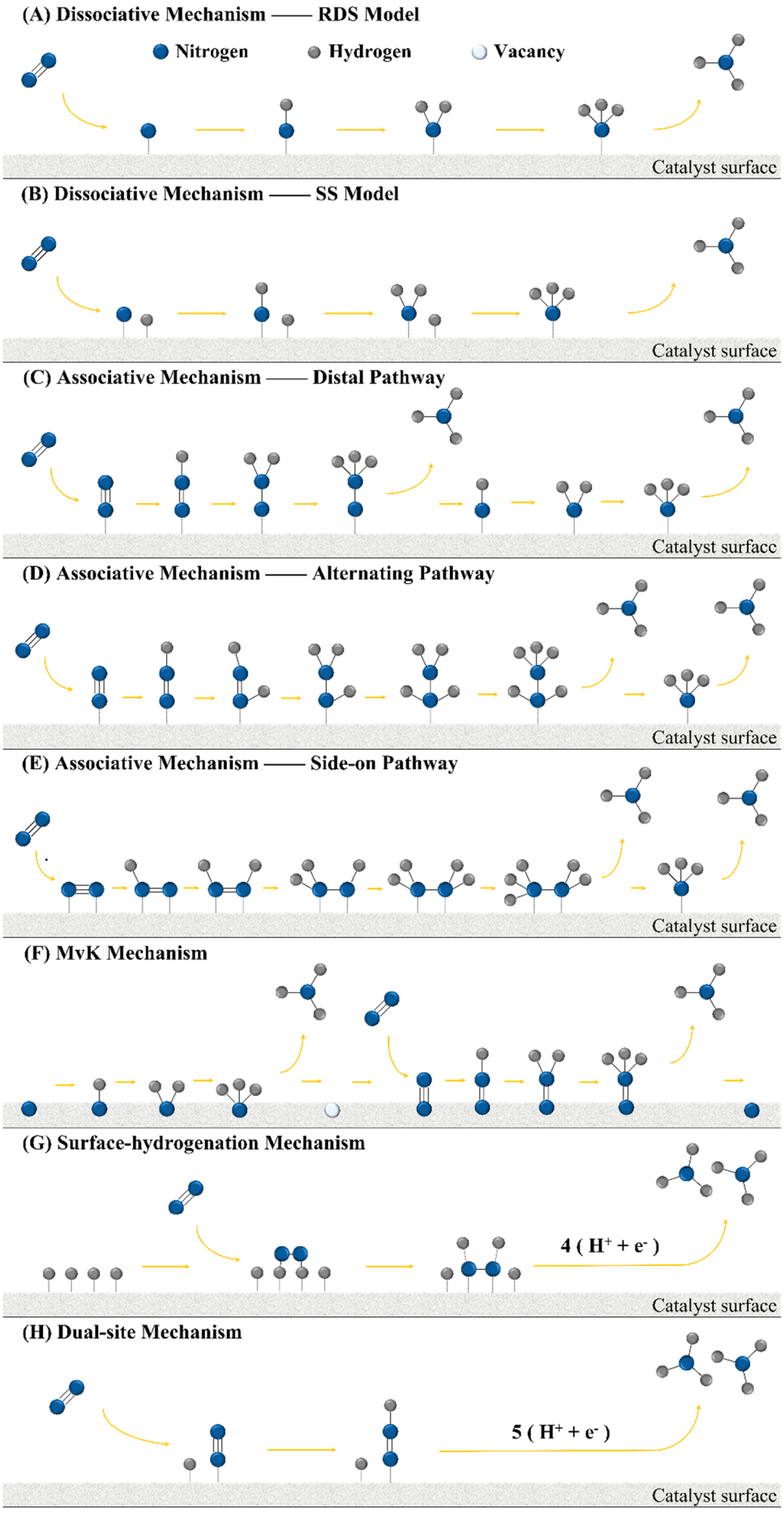

Figure 4. Different mechanisms of N_2RR.

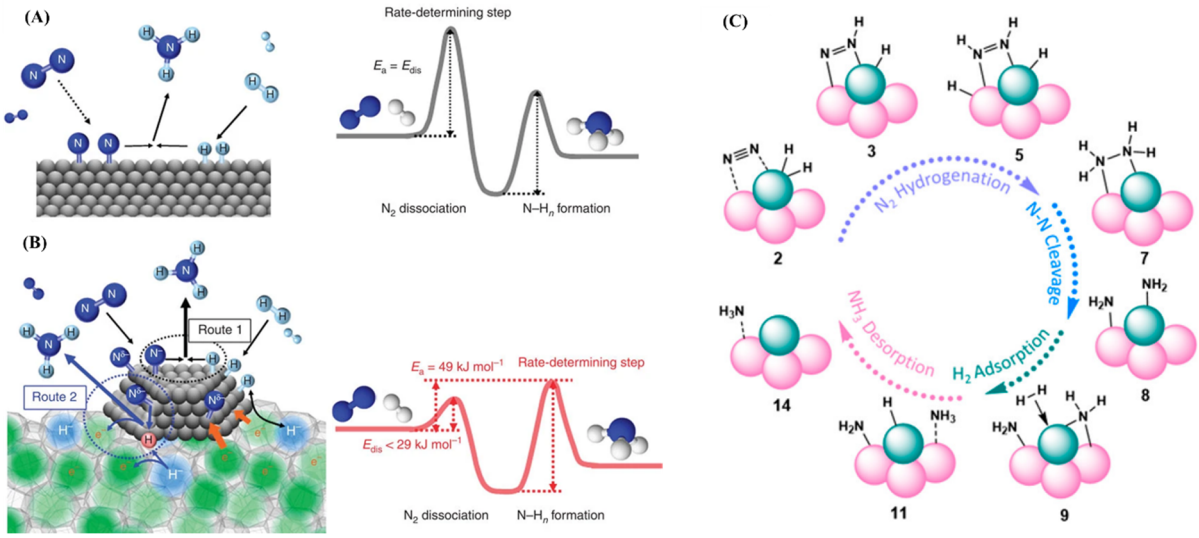

Figure 5. Reaction mechanism and energy profile for ammonia synthesis over (**A**) conventional catalyst and (**B**) Ru/$C_{12}A_7$:e^-. (**C**) Mechanism on the singly dispersed bimetallic site of Rh_1Co_3. Reprinted with permission from Ref. [41]. Copyright © 2015, Springer Nature. Reprinted with permission from Ref. [56]. Copyright © 2018, American Chemical Society.

2.2.2 Associative Mechanism

Li's group identified the thermal synthesis of ammonia on Rh_1Co_3 [56] and Fe_3 [57] clusters as proceeding via an associative mechanism, rather than dissociative. This involves H_2 chemisorption (with initial H_2 dissociation), N_2 protonation, and then triple bond dissociation, with N_2 protonation being the RDS (Figure 5C). The associative mechanism is also prevalent in electrocatalytic reactions [58]. In this context, the triple bond rupture occurs only after NH_3 formation (differing from Li's group where dissociation happens during the N_2H_4 step). However, initial N_2 activation, a critical step for inert N_2, occurs similarly. In the associative distal pathway, N_2 adsorbs vertically on the catalyst surface. Protons preferentially attack the terminal nitrogen atom, leading to three hydrogenations before triple bond breakage and release of one ammonia molecule. Subsequent protonation of the remaining nitrogen atom liberates the second ammonia molecule. In the associative alternating pathway (Figure 4D), N_2 is also adsorbed perpendicularly. Protons sequentially attack the upper and lower nitrogen atoms. After the fifth hydrogenation, the upper nitrogen atom, bonded to three hydrogens, is released as NH_3 by breaking the triple bond. The sixth hydrogenation step then liberates the second NH_3 molecule.

Regarding the side-on pathway (Figure 4E, states E4–E8), some researchers have inaccurately termed it the "enzyme mechanism" (states E0–E8), a term rooted in biological research where nitrogenase activity remains poorly understood [21,59,60]. While some electrocatalytic reactions follow this path [61,62], the nitrogen molecule lies flat on the catalyst surface and undergoes sequential hydrogenation from left to right. Similar to the alternating pathway, the first ammonia is released after the fifth hydrogenation, and the second after the sixth. As triple bond cleavage occurs after NH_3 generation, this is classified as an associative mechanism in this review.

2.2.3. Mars-Van Krevelen Mechanism

On transition metal nitride surfaces, the Mars-van Krevelen (MvK) mechanism (Figure 4F) may operate. Surface nitrogen atoms are sequentially hydrogenated to form the first NH_3 molecule, leaving an N vacancy that serves as an adsorption site for subsequent N_2 molecules. The second ammonia molecule is produced by terminal hydrogenation, again leaving a nitrogen atom that cycles within the lattice. This pathway can potentially degrade the catalyst lattice, posing challenges for long-term stability [24].

2.2.4. Surface-Hydrogenation Mechanism

The surface-hydrogenation mechanism (Figure 4G) is a novel pathway observed with precious metal catalysts [63]. Researchers found that the lower onset potential originates from the Volmer step of HER rather than N_2 activation. The catalyst surface first adsorbs hydrogen, providing electrons to the catalyst and nitrogen and creating vacant orbitals for N_2 lone pair acceptance. N_2 is activated by two surface *H

atoms, lying flat on the surface. The transition state is $*H_2N_2$ (with H between the catalyst and N), which then transforms into the final adsorption state $*H_2N_2$ (with N in the middle). Ammonia is subsequently formed through four exothermic and spontaneous PECT steps. This mechanism highlights that hydrogen adsorption is inevitable and potentially rate-limiting, while also facilitating N_2 activation.

2.2.5. Dual-Site Mechanism

Before activating N_2 (states E0–E4), nitrogenase adsorbs 4H to form two bridged hydride intermediates (E4, 4H) for proton and electron storage. This is followed by H_2 release through reduction and elimination, exposing an active site for N_2 binding or forming another hydride [59,64–66]. The dual-site mechanism (Figure 4H) is the bioinspired pathway most closely resembling nitrogenase [67,68] and also suggests that hydrogen adsorption is beneficial, consistent with the surface-hydrogenation mechanism. Here, H and N_2 attach to different active sites, initially approximating the SS model. *H desorbs from its site and moves to a neighboring nitride intermediate, generally considered the RDS, followed by five PECT steps to produce NH_3.

Mechanisms where triple bond dissociation occurs after NH_3 formation are termed dual-site associative pathways, while the SS model can be considered a dual-site dissociative pathway. The scaling relationships typically hinder reaction intermediates like $*N_2H$ and *NH [38]. However, dual-site activation can overcome these limitations and successfully reduce the energy barrier [55,69]. Stoukides' group has reported the influence of H_2 partial pressure on NH_3 production rates in electrocatalytic experiments under high temperature and atmospheric pressure [70–74]. Across research on nitrogenase, industrial catalysts, and electrocatalysis, there is a growing emphasis on the role of hydrogen over nitrogen in N_2RR. The SS model, surface-hydrogenation, and dual-site mechanisms represent recent advancements. Consistently, a dual-site pathway involving hydroxylation for H adsorption and Ti for N_2 adsorption has been studied in TiO_2 photocatalytic nitrogen reduction for ammonia production [75,76]. These mechanistic studies offer valuable insights.

2.3. The Relationship between N_2OR and OER

The N_2OR process can be readily understood with N_2RR knowledge as a foundation, differing primarily in being an anodic, electron-losing reaction. Both N_2OR and its competitive reaction, OER, involve four steps of hydroxyl-related electron loss (RHLE), requiring significant overpotentials to initiate. The Pourbaix diagram [18] shows that their potential lines are closely spaced, with theoretical potential intervals for N_2OR. However, the inherent similarity between the competing adsorbate elements, O and N (adjacent in the same periodic table period), makes averting their competitive relationship more challenging. The anodic reaction equations are as follows:

Under acidic conditions:

$$N_2OR: N_2 + 2H_2O - 4e^- = 2NO + 4H^+ \quad (11)$$

$$OER: 2H_2O - 4e^- = O_2 + 4H^+ \quad (12)$$

Under alkaline conditions:

$$N_2OR: N_2 + 4OH^- - 4e^- = 2NO + 2H_2O \quad (13)$$

$$OER: 4OH^- - 4e^- = O_2 + 2H_2O \quad (14)$$

The production of nitric acid from N_2OR is generally considered to proceed in two steps, both linked to the OER side reaction [34,77]. The first step (reaction 11 or 13) involves the electrochemical conversion of N_2 to an active NO intermediate, which is also involved in OER. The subsequent step is typically a spontaneous, non-electrochemical process where *NO reacts with H_2O and $*O/O_2$ to form nitric acid, as described by reactions (15) and (16). It is important to note that $*O/O_2$ is supplied by secondary reactions, similar to the combination of reactions (5) and (6). The crux of current research lies in understanding the initial electrochemical step: how N_2 is transformed into NO.

$$*NO + *O + H_2O \rightarrow HNO_3 \quad (15)$$

$$*NO + O_2 + H_2O \rightarrow HNO_3 \quad (16)$$

2.4. Mechanisms of N_2OR

Current DFT calculations for N_2OR mechanisms are quite complex. Summarizing these with simulated atomic diagrams is premature; this section outlines some typical mechanisms for comprehension. ∗NO is a crucial reaction intermediate, and the close electronegativity of N and O leads to ongoing debate regarding N_2 oxidation activation methods. Therefore, mechanisms are tentatively categorized into N-preferred and O-preferred pathways.

2.4.1. O-Preferred Mechanism

Yuan investigated the N_2 and H_2O reaction pathway in photosynthesis (Figure 6A) [78], following a H_2O-H_2O-N_2 adsorption sequence. The TiO_2 surface first adsorbs H_2O, then removes 2H, and circulates once again to generate two ∗O. N_2 is activated by ∗O, adsorbing flat onto it to form 2(∗ON), followed by nitric acid generation via reaction (16). Comer employed a Bayesian Error Estimation Functional (BEEF-vdW) based model to calculate overpotentials for N_2RR and N_2OR on TiO_2(110). They found that the thermodynamic limit potential for N_2OR is lower, proceeding via a H_2O-N_2-H_2O adsorption sequence to generate 2NO, as shown in Figure 6B [79].

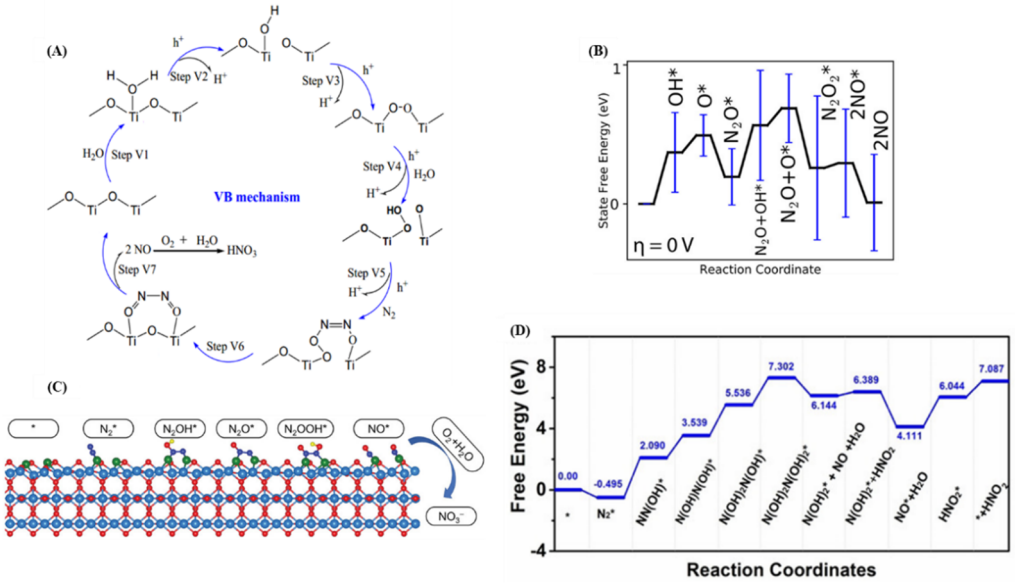

Figure 6. O-preferred mechanism of (**A**) H_2O-H_2O-N_2 and (**B**) H_2O-N_2-H_2O adsorption sequence. N-preferred mechanism (**C**) and (**D**). Reprinted with permission from Ref. [78]. Copyright © 2013, Springer Nature. Reprinted with permission from Ref. [79]. 2018, American Chemical Society. Reprinted with permission from Ref. [80]. Copyright © 2020, Wiley.

2.4.2. N-Preferred Mechanism

Xie's group reported that the Gibbs free energy for the N-preferred pathway, where N_2 first adsorbs on WO_3 surface cavities, is lower than that of the O-preferred pathway without holes. N_2 is more easily activated and transformed into ∗NO, which then spontaneously forms nitric acid with O_2 and H_2O [81]. The N-preferred mechanism, characterized by initial N_2 adsorption on the catalyst surface, involves subsequent steps that vary, following pathways such as the one in Figure 6C. N_2 adsorbs flat on the surface ($N_2 + * \rightarrow *N_2$), then adsorbs OH^- and loses an electron ($*N_2 + OH^- - e^- \rightarrow *N_2OH$), a step considered the RDS. It then reacts with OH^-, losing another electron and forming H_2O ($*N_2OH + OH^- - e^- \rightarrow *N_2O + H_2O$). Subsequently, two RHLE steps occur to form the second ∗O ($*N_2O + OH^- - e^- \rightarrow *N_2O(OH)$, $*N_2O(OH) + OH^- - e^- \rightarrow 2*NO + H_2O$). This requires a total of 4 OH^- and involves the loss of $4e^-$ (4 RHLE steps) to produce 2(∗NO) [25,34,77]. Figure 6D illustrates a pathway resembling the associative alternating mechanism, where OH^- adsorption follows N_2 adsorption. N_2 stands vertically on the surface, and OH^- is added sequentially from top to bottom with electron loss, proceeding through 4 RHLE steps to form 2NO. The RDS remains the hydroxylation of $*N_2$ to form $*N_2OH$ ($*N_2 + OH^- - e^- \rightarrow *N_2OH$) [80].

In summary, secondary reactions appear vital for EN_2F. The N_2OR process, irrespective of O-preferred or N-preferred pathways, involves 4 RHLE steps, with the generation of $*N_2OH$ often identified as the RDS.

OH^- adsorption aids in activating or polarizing N_2, thus catalysts require some OER activity. Once *NO is formed, $*O/O_2$ from OER is still needed for spontaneous conversion to HNO_3. Active sites with identical adsorption energies may not be optimal for reactions with multiple intermediates [82–84]. Despite computational limitations (theoretical methods, model accuracy, and strategies) leading to mechanistic uncertainty [85], N_2RR research has advanced to focus on H dissociation and adsorption pathways. N_2OR, however, remains at a more nascent stage. The close properties of N and O (atomic radius, electronegativity) make distinguishing competitive adsorption challenging, a complexity requiring progressive refinement.

3. Advanced Catalysts

3.1. Scaling Relationships

The adsorption energy of nitrogen on the catalyst surface serves as a quantitative descriptor for EN_2F activity. Intermediates from different elementary steps often share similar surface adsorption bonds, such as $*N_aH_b$ in N_2RR and $*N_xO_y$ in N_2OR, both featuring N-catalyst (*N) bonds. A fundamental challenge in EN_2F is that intermediate combinations tend to follow conventional linear relationships, implying a single variable influences the entire reaction [86]. Ideally, active site design should promote diversified binding configurations for these intermediates. For instance, multi-site functionalization, where transition states or intermediates of elementary steps interact with the catalyst surface via different active sites, can generate two or more independent descriptors [38,87]. Mechanisms like MvK, surface-hydrogenation, and dual-site pathways offer potential routes to circumvent scaling relation limitations, thereby achieving unprecedented selectivity and activity. For N_2RR, as exemplified in Figure 7A,B, advanced strategies should selectively stabilize $*N_2$ or $*N_2H$ intermediates while destabilizing $*NH_2$ or *NH [38,61,69].

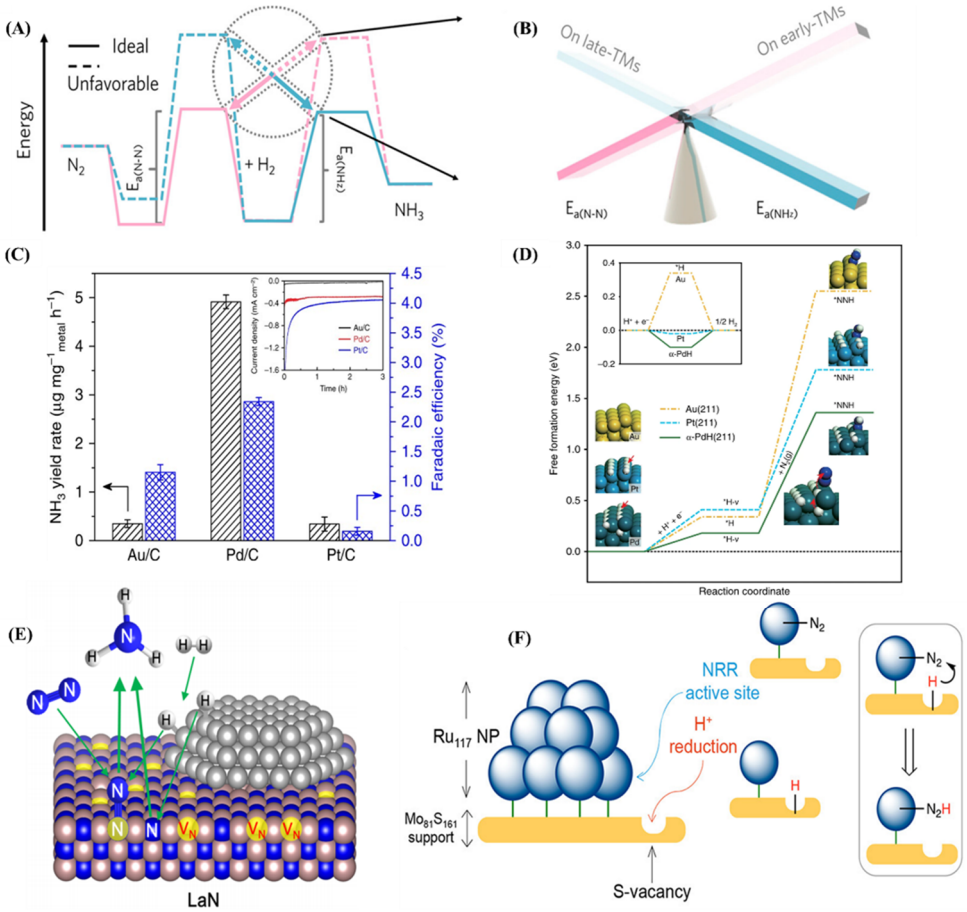

Figure 7. (**A**) Schematic free-energy diagram for ammonia synthesis on strong (pink) and weak (blue) N-bonding catalysts. (**B**) The scaling relationship depicting Ea(N-N) and Ea(NHz) on the two sides of a seesaw. Comparison of the Pd/C with Au/C and Pt/C catalysts by (**C**) experiment and (**D**) DFT calculation. Reaction mechanisms of (**E**) Ni/LaN and (**F**) Ru/MoS2. Reprinted with permission from Ref. [69]. Copyright © 2018, American Chemical Society. Reprinted with permission from Ref. [88]. Copyright © 2020, American Chemical Society. Reprinted with permission from Ref. [55]. Copyright © 2018, Springer Nature. Reprinted with permission from Ref. [89]. Copyright © 2020, Springer Nature.

3.2 Advanced Catalysts for N_2RR

While some electrocatalysts enhance N_2RR performance, they often also improve HER performance, evidenced by increased current, decreased Tafel slope, altered valence band structure, and optimized H_2O/H adsorption energy [90,91]. Suppressing side reactions can boost Faradaic Efficiency (FE) but may lower yields, thus hindering N_2RR activity; a suitable proton donor is consequently necessary [36]. Notably, the Volmer step contributes to N_2 hydrogenation, a phenomenon explained by the surface-hydrogenation and dual-site mechanisms. This section introduces related catalysts, including strong and weak N-bonding dual-site catalysts, which help mitigate proportional relationships.

3.2.1. Catalysts of Surface-Hydrogenation Mechanism

Prior to Wang's group proposing the surface-hydrogenation mechanism [63], Feng's group introduced a similar Grotthuss-like hydride transfer pathway [89]. Their Pb/C catalyst exhibited the highest yield and FE at a low potential of 56 mV, with surface chemical hydrogenation as the rate-determining step (RDS). Experimental results (Figure 7C) indicated that Au and Pt catalysts yielded an order of magnitude less NH_3 than Pb. DFT calculations (Figure 7D) attributed this to the excessive HER activity of Pt and inhibited H adsorption on Au, while Pb's activity stemmed from inhibited ∗H desorption [89]. Calculating the free energy for the RDS, Wang found the yield order to be hcp Au > fcc Au > fcc Pb [63]. Despite slight differences in results, the reaction pathways are comparable. Recently, Cheng directly prepared $PbH_{0.43}$ using in-situ H_2 injection and employed isotopic hydrogen labeling to confirm that lattice hydrogen served as the proton source for N_2RR. In-situ Raman and DFT studies revealed $*N_2H$ formation as the RDS, with H_2 injection reducing activation energy, consistent with the surface-hydrogenation mechanism [92].

3.2.2. Catalysts of Dual-Site Mechanism

Building upon industrial HB reaction research, Honoso's group has extensively studied metal cluster support catalysts. Since 2017, they have focused on hydrides as carriers [51–54], replacing $C_{12}A_7{:}e^-$ (studied for over a decade [45]), while seeking novel H- and N3- conductor materials [49,50,53,93]. Their work emphasizes dual-site pathways [53,55], exemplified by catalysts like Ru/BaO-CaH_2 [51], Ru/Ca_2NH [52], TM/$BaCeO_{3-x}N_yH_z$ [53], Ru/CaFH [54] and Ni/LaN [55]. The Ni/LaN catalyst, conceptualized with dual active sites, was developed (Figure 7E). Ni possesses strong H_2 activating ability but weak N binding, whereas LaN, as a carrier, utilizes numerous N vacancies to activate N_2 [55]. Similar industrial studies include Ru/LaN/ZrH_2 [94] and Fe/$TiO_{2-x}H_y$ [69]. In recent years, dual-site catalysts have demonstrated excellent performance in various electrocatalytic reactions, including HER [95], ORR [96], CO_2RR [97]. Due to its tunable HER activity, MoS_2 is frequently utilized as a unique carrier in N_2RR. While 2H-MoS_2 with a S-wrapped structure shows weak catalytic activity, removing a sulfur atom to form a semi-open configuration offers a convenient activation strategy [68].

A highly selective Ru/MoS_2 polycrystal N_2RR catalyst was prepared by Suryanto, which could inhibit the reduction of H^+ and provided binding sites for N_2 activation through the modification of Ru clusters (Figure 7F). Theoretical calculation suggested that the high activity resulted from synergistic interactions, with Ru clusters acting as N-binding sites and hydrogenated S-vacancies playing an important role as H-providers, that formed ∗H can transfer to the adjacent $*N_2$ directly, $Ru*N_2$ + S-vac∗H ⇌ $Ru*N_2H$ [88]. The Co/MoS_{2-x} polycrystalline nanosheet studied by Zhang were different from Suryanto in terms of adsorption site. The S at the edge adsorbed H while the n-type S vacancy was rich in electrons, which can donate electrons to the HOMO of N_2. The presence of Co atom next to the S vacancy reduced the barrier for N_2 activation and improved the yield of NH_3 at low voltage. The authors believe that the catalyst is a model of the inorganic framework of the nitrogenase cofactor [68].

A highly selective Ru/MoS_2 polycrystal N_2RR catalyst prepared by Suryanto inhibited H^+ reduction and provided N_2 activation sites through Ru cluster modification (Figure 7F). Theoretical calculations indicated that high activity resulted from synergistic interactions, with Ru clusters acting as N-binding sites and hydrogenated S-vacancies playing a crucial role as H-providers. The resulting ∗H could directly transfer to adjacent $*N_2$ ($Ru*N_2$ + S-vac∗H ⇌ $Ru*N_2H$) [88]. Zhang's study on Co/MoS_{2-x} polycrystalline nanosheets differed from Suryanto's regarding adsorption sites. Here, sulfur at the edge adsorbed H, while n-type S vacancies, electron-rich, donated electrons to the N_2. The presence of Co atoms adjacent to S vacancies lowered the N_2 activation barrier and enhanced NH_3 yield at low voltage. The authors proposed this catalyst as a model for the inorganic framework of the nitrogenase cofactor [68].

Kim clearly established the dual-site mechanism as a biomimetic N_2RR pathway. Investigating a $Cu_{1.81}S$ catalyst, the study found that N_2 activation originated from three-coordinated Cu sites, with sulfur acting as the H adsorption site ($Cu{*}N_2 + S{*}H \rightleftharpoons Cu{*}N_2H$). These sites facilitate proton transfer to N_2 and stabilize the intermediate N_2Hx through N-H…S hydrogen bonding, significantly reducing the reaction overpotential. This N_2 protonation process closely resembles that of nitrogen fixation enzymes [67]. Besides sulfide carriers, VN_3/hydrogenated graphene has also been explored [98]. The synergistic effect between the support and metal effectively overcomes scaling relationships, promoting further catalyst design exploration.

3.2.3. Catalysts of Strong and Weak N-Bonding Pair

The dual-metal ammonia synthesis catalysts were investigated by Jacobsen in 2001. He identified a volcano activity map (Figure 8A) where the optimal nitrogen adsorption energy was achieved by combining Mo (strong N binding) and Co (weak N binding) [99]. The Rh_1Co_3 cluster mentioned earlier falls into this catalyst class [56]. Computational chemistry studies have indicated that bimetallic catalysts are more suitable for N_2RR than monometallic ones [100]. Du's group calculated five monometallic elements (Fe, Co, Mo, W, Ru) and their bimetallic combinations (Figure 8B), finding clear scaling relationship limitations for monometallics. In contrast, bimetallic dimer catalytic sites partially circumvented these obstacles, demonstrably reducing the hydrogenation free energy barrier by twofold [62]. Wang's group performed similar calculations for the same objective [101].

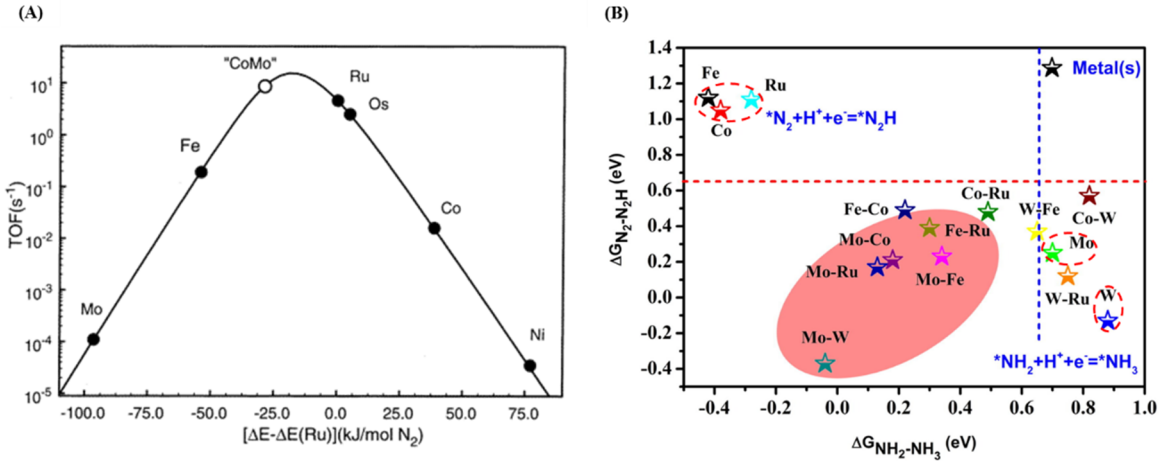

Figure 8. (**A**) Volcano activity map of the adsorption energy of nitrogen. (**B**) Gibbs free energy changes for the first and last hydrogenation steps of N_2RR on different catalysts. Reprinted with permission from Ref. [102]. Copyright © 2001, American Chemical Society. Reprinted with permission from Ref. [62]. Copyright © 2020, Elsevier.

Employing advanced characterization techniques (XANES, EXAFS, XPS, EELS), catalysts featuring metal-metal electron transfer, such as AuNi/NC [103], PbCu/NC [104], FeMo/NC [105], $FeCu/C_3N_4$@CNT [106], FeAg/Si [107], have been experimentally synthesized and characterized for N_2RR. The electron-rich metal in bimetallic pairs polarizes electron-deficient N_2, facilitating subsequent proton addition. These reactions follow the associative mechanism and effectively suppress side reactions. The nearby metals, exhibiting different N atom adsorption energies, function as potential catalysts for improving scaling relationships. However, for optimal effectiveness, the metal diatomic distance must be extremely close to the N≡N bond length (Å level) [108], making precise synthesis and characterization exceptionally challenging [109]. Similarly, the electron transfer pair between non-metallic B and metallic Mo can simultaneously activate both nitrogen atoms in N_2 [110]. The specific activation mechanism will be detailed in Section 4.4.

3.3. Advanced Catalysts for N_2OR

For N_2OR, the adsorption of OH^- as a byproduct also promotes N_2 activation, and this side reaction is beneficial [34,77]. Kuang prepared Ru/TiO_2 catalysts, where DFT revealed that Ru doping into the TiO_2 lattice altered Ru oxidation states (from Ru4+ to Ruδ+, the main active site). This modification enhanced the electrochemical conversion rate of the first N_2OR step ($N_2 \rightarrow {*}NO$). The additional formation of Ru4+, possessing high OER activity, could promote the *NO intermediate to generate NO_3^-, with $2.79Ru/TiO_2$ exhibiting the best EN_2F performance compared to $0.36Ru/TiO_2$ and $5.41Ru/TiO_2$ [77]. Dai prepared a

series of $ZnFe_xCo_{2-x}O_4$ spinel oxides; among them, $ZnFe_{0.4}Co_{1.6}O_4$ and $ZnFe_2O_4$ displayed the highest and lowest N_2OR activity, respectively, consistent with their OER activity trends. Fe, as an active site, contributed to the formation of the first NO bond. EXAFS showed that the introduction of $Fe_{0.4}$ led to the highest valence state of Co (Co^{4+}), which, with emptier 3d orbitals, could strongly interact with O 2p, aiding stable OH^- adsorption for subsequent NO_3^- generation. This study highlights the synergistic advantages of Fe and Co in adsorbing oxygen-containing species [111].

The consistent conclusion can also be drawn according to the experimental results that proper regulation of OER side reactivity can also promote N_2OR. The key is that the adsorbed OH^- ions must be successfully bonded to the N to avoid the dominance of competing OER. As the voltage increases, the selectivity of N_2OR goes down, and there's an optimal potential just like N_2RR. The following Table 1 lists the current NO_3^- yield and efficiency of N_2OR, which has been studied in relatively few articles. It is noteworthy that Fe-SnO_2 is a bifunctional EN_2F catalyst, and the O vacancy (or Fe adjacent to O vacancy) can effectively adsorb and activate N_2, with N_2RR yield and FE both greater than N_2OR [80], which may be due to the large difference between the adsorption of H^+ and OH^- by this catalyst.

Table 1. Performance of different catalysts for N_2OR reported.

Catalyst [Ref.]	Electrolyte	NO_3^- ions Formation Rate	Faradaic Efficiency, %	Potential, V vs. RHE
Ru/TiO_2 [77]	0.1 M Na_2SO_4	161.9 μmol h^{-1} g^{-1} 10.04 μg h^{-1} mg^{-1}	 26.10	2.2 1.8
Pd-MXene [34]	0.01 M Na_2SO_4	2.8 μg h^{-1} mg^{-1} 45.16 μmol h^{-1} g^{-1}	11.34	2.03
$ZnFe_{0.4}Co_{1.6}O_4$ [111]	1 M KOH	130 ± 12 μmol h^{-1} g^{-1}	1.62 ± 0.34	1.6
$ZnFe_2O_4$ [111]		26.4 ± 1.9 μmol h^{-1} g^{-1}	10.1 ± 0.9	1.5
Pt [25]	0.3 M K_2SO_4	0.06 μmol h^{-1} cm^{-2}	1.23	2.13
Fe-SnO_2 [80]	0.05 M H_2SO_4.	42.9 μg h^{-1} mg^{-1}	0.84	1.96
Pd-s PNSs [112]	0.1 M KOH	18.56 μg h^{-1} mg^{-1}	 2.5	1.75 1.55

Experimental results consistently indicate that proper regulation of OER side reactivity can also promote N_2OR. The key lies in ensuring adsorbed OH^- ions successfully bond with N, avoiding the dominance of competing OER. As voltage increases, N_2OR selectivity decreases, implying an optimal potential, similar to N_2RR. Table 1 summarizes the reported NO_3^- yields and efficiencies for N_2OR, an area with relatively few studies. Notably, Fe-SnO_2 serves as a bifunctional EN_2F catalyst, where oxygen vacancies (or Fe adjacent to O vacancy) effectively adsorb and activate N_2. This catalyst shows greater N_2RR yield and FE than N_2OR [80], potentially due to significant differences in H^+ and OH^- adsorption by this material.

Thanks to the progress of research of nitrogenase and the understanding of traditional scaling relationship, the study of heterogeneous catalysts has been accelerated. The surface-hydrogenation mechanism and the dual-site mechanism (biomimetic mechanism) proposed in electrocatalytic systems recently can also prove the importance of side reactions. In future EN_2F catalytic studies, the activity of the side reactions should be properly considered to obtain suitable selectivity and yield.

The progress in nitrogenase research and the understanding of traditional scaling relationships have accelerated heterogeneous catalyst studies. The proposed surface-hydrogenation and dual-site (biomimetic) mechanisms in electrocatalytic systems also underscore the importance of side reactions. Future EN_2F catalytic studies should appropriately consider side reaction activity to achieve optimal selectivity and yield.

4. The Kinetic Steps of EN_2F

The N_2 molecule possesses a stable, closed-shell electron configuration with three pairs of 2p orbitals shared between the two N atoms. Its large HOMO-LUMO energy gap (10.8 eV) results in a strong N≡N triple bond. Consequently, electron transfer is difficult [113]. The triple bond's high energy (941 kJ/mol) and the low proton affinity (493.8 kJ/mol) hinder protonation. N_2 is nonpolar, has a high ionization potential (15.841 eV), and a low electron affinity (−1.903 eV). These factors contribute to its use as a chemically inert atmosphere [21]. Furthermore, N_2's low solubility and diffusion coefficient significantly impact EN_2F dynamics [114]. Several initial kinetic steps of EN_2F are discussed below, including dissolution, mass transfer, adsorption, and activation, to better understand and address related challenges.

4.1. Dissolution of N_2

Water is a common solvent under mild conditions. N_2 exhibits the lowest solubility among common gases in water (Figure 9A), with a molar solubility ratio of approximately 1:100000. O_2 and NO are roughly twice and three times more soluble, respectively [115]. Methanol exhibits a 10-fold increase in N_2 solubility compared to water [116]. Increasing the overall N_2 concentration in the electrolyte enhances ammonia selectivity in N_2RR [117]. N_2 dissolution is the initial kinetic step for both N_2RR and N_2OR, and improving its solubility is crucial for increasing the rate of EN_2F.

Aprotic ionic liquids offer a promising alternative, miscible with trace water to suppress HER and OER side reactions. Electrolyte properties like viscosity, conductivity, and N_2 solubility can be tuned by adjusting the ionic liquid salt concentration [118,119]. MacFarlane's group demonstrated that highly fluorinated solvents exhibit high N_2 solubility (e.g., perfluoro heptane's N_2 solubility is 25 times that of water). Increasing the proton source concentration increased both N_2RR and HER currents, leading to an optimal potential of −0.65 V (Figure 9B) [118]. Comparing three hydrophobic ionic liquid salts, the FE trend mirrored their N_2 solubility, highlighting the importance of solubility [120]. N_2 solubility was linearly correlated with the volume fraction of fluorinated solvents [121].

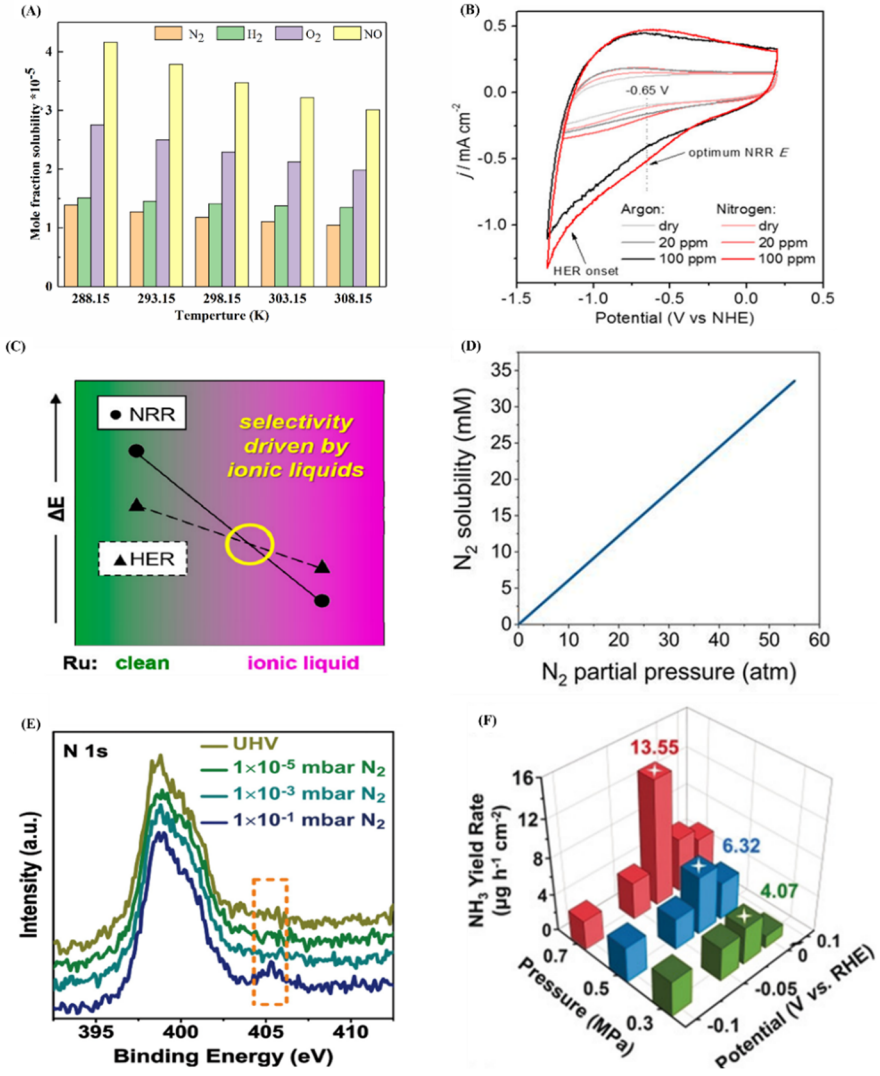

Figure 9. (**A**) Solubility comparison of different gases at different temperatures [115]. (**B**) Cyclic voltammogram in the presence of N_2 and Ar gases with various concentration of the proton source. (**C**) Relative energy differences for N_2RR and HER in the absence and presence of ionic liquid. (**D**) A plot of the solubility of N_2 gas versus the partial pressure. (**E**) Near-ambient pressure X-ray photoelectron spectroscopy of N 1s on catalyst. (**F**) NH_3 yield rate of catalyst versus different pressure and potential. Reprinted from Refs. [118,122]. Copyright © 2018, 2019 American Chemical Society. Reprinted from Ref. [123]. Copyright © 2020, National Academy of Sciences. Reprinted from Ref. [124]. Copyright © 2019, Wiley. Reprinted from Ref. [105]. Copyright © 2019, Elsevier.

While the specific role of ionic liquids remains under investigation, Ortuño and López used theoretical calculations to understand the ionic liquid-modified Ru catalyst surface and the $*N_2H$ intermediate at the atomic scale. Their results suggest that the metal-ionic liquid interface can bypass linear scaling relationships and enhance selectivity (Figure 9C) [122].

Pressurization significantly aids EN_2F. N_2 solubility is proportional to its partial pressure in water within a certain range (Figure 9D) [123]. Han's group used in-situ near-ambient pressure XPS to detect N_2-catalyst interactions at different partial pressures and room temperature, observing gradual N_2 detection in the N 1s spectrum from ultra-high vacuum to saturation (Figure 9E) [105]. Wang's group found that increasing the pressure to 0.7 MPa reduced the reaction overpotential (Figure 9F) [124]. Duan's group conducted experiments at 55 atm, improving both selectivity and yield [123]. This strategy offers several advantages: (1) N_2RR involves volume shrinkage as NH_3 exists as NH_4^+ in aqueous solution, and pressurization shifts the equilibrium forward; (2) the HER side reaction increases volume, and pressurization inhibits it, improving main reaction selectivity; (3) pressurization enhances N_2 solubility [124]. Interestingly, these advantages also apply to N_2OR, as the product NO exists as NO_3^-, and the secondary reaction produces O_2 with volume expansion. However, pressurized operation requires reactor tightness beyond that of ordinary reactors.

Gas solubility is also temperature-dependent, leading to the use of heating devices in some experiments [88,125]. While increased temperature accelerates gas diffusion, it can also reduce N_2 solubility, requiring careful consideration.

4.2. Mass Transfer of N_2

Besides low solubility, the diffusion coefficient of N_2 in aqueous electrolytes ($D_{N2} = 2 \times 10^{-9}$ m^2 s^{-1}) is approximately 1/5 that of protons ($D_{H^+} = 9.3 \times 10^{-9}$ m^2 s^{-1}) [114]. Electrolytic cell configuration affects N_2 diffusion and transfer. Most EN_2F experiments use single-chamber [125,126] or H-type electrolytic cells [127]. The close proximity of electrodes in single-chamber cells can lead to product reaction at the counter electrode and counter electrode reactions jeopardizing the catalyst or becoming competing reactions [127]. Graphite is commonly used as the counter electrode due to Pt dissolution and deposition, but recent research indicates that graphite hinders accurate electrocatalytic performance evaluation. H-type cells physically separate the anode and cathode compartments, effectively avoiding activity underestimation [128] and inhibiting proton and electron transmission, improving selectivity compared to single-chamber cells [126]. However, membrane pretreatment is crucial to eliminate interference from active nitrogen contamination [129,130]. Furthermore, the electrolyte in these cells is typically static, resulting in high N_2 mass transfer resistance.

N_2 depletion or spillover near the electrode during the reaction limits the rate of EN_2F. Increasing N_2 coverage on the catalyst surface can inhibit core actant adsorption and improve selectivity (Figure 10A) [131]. Flow reactors overcome the mass transfer limitations of static batteries by continuously circulating reactants and products in and out of the electrolytic pool, significantly increasing the current. Two common structures for EN_2F are the gas diffusion electrode (GDE) and the microfluidic flow cell (Figure 10B,D) [132,133]. The feed gas passes through the GDE, ensuring sufficient contact with the catalyst to increase N_2 coverage, which can be adjusted by the N_2 partial pressure. Chen improved GDE (Figure 10B) by adding an extra gas diffusion layer between the catalyst and the separator to further improve the selectivity and then did a series of studies on N_2RR [134–137]. Cui found that FE dropped from 8.28% to 2.74% after 16h of potentiation electrolysis using ordinary GDE (only one gas diffusion layer), attributing this to the decay of the catalyst and the changes in water content and conductivity in the Nafion membrane [138]. While, a recent workshop on the website by Cui clarified the phenomenon of GDE more clearly: a small amount of water droplets can be seen on the side of the gas diffusion layer as it penetrates into the cathode chamber by pressure. It just so happens that Chen's additional gas diffusion layer can alleviate this problem of penetration to a certain extent [135–137]. A novel microtubular gas diffusion electrode (Figure 10C) was prepared directly and applied at 0.3bar N_2 in H-type cell in order to enhance the transmission of N_2 [139].

The microfluidic flow battery, in which driving the electrolyte to flow not only promotes the mass transfer of nitrogen but also avoids the accumulation of products such as NH_4^+ and NO_3^-, and shifts the reaction equilibrium to the positive direction, which is currently the most advanced battery configuration Li [133], and Liu [140] increased the current density by using the flow electrolytic cell, and the efficiency and yield of N_2RR raised in multiples. The structure may also cause electrolyte penetration due to osmotic pressure, resulting in performance degradation. In addition, a pump is prerequisite to drive the flow of electrolyte, which requires strict airtightness. At the same time, different requirements on the shape and stability of the working electrode, reference electrode and counter electrode, lead the whole battery system

to make it expensive and complex to operate. Finally, it should be noted that the voltage [141] and pH [142] at the interface of the flow cell changes significantly. While, because of the straightforward doubling of performance, flow cell can be constructed and executed in a laboratory, and their design can be more availably expanded to commercial grade reactor as the technology evolves [132].

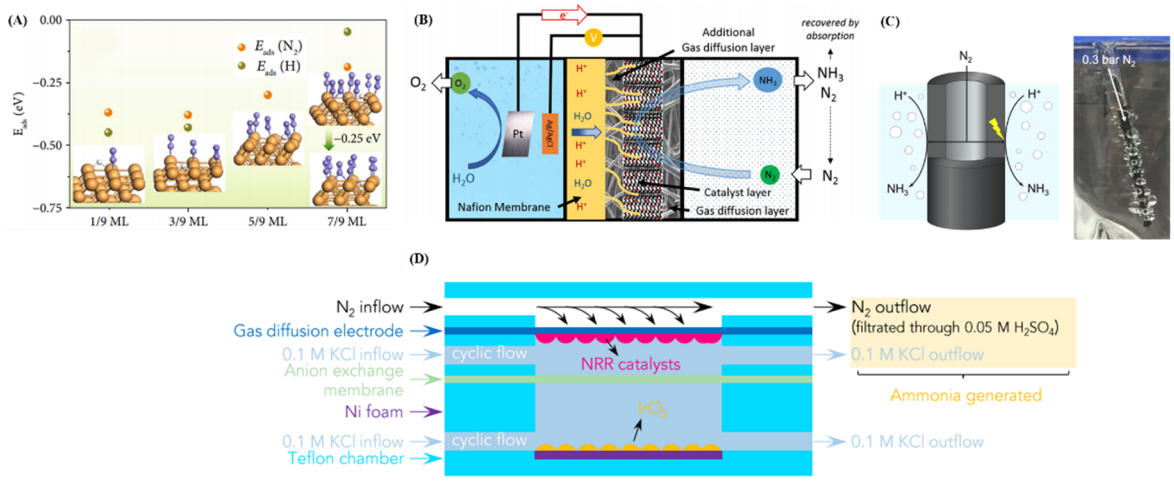

Figure 10. (**A**) The influence of different N_2 coverage on the adsorption energy of N_2 and H. Schematic view of interior configuration of (**B**) the membrane flow cell, (**C**) microtubular gas diffusion electrode and (**D**) microfluidic flow cell. Reprinted with permission from Ref. [131]. Copyright © 2019, AAAS. Reprinted with permission from Ref. [135]. Copyright © 2017, American Chemical Society. Reprinted with permission from Ref. [139]. Copyright © 2020, Wiley. Reprinted with permission from Ref. [133]. Copyright © 2020, Cell Press.

Performance of different flow cells for N_2RR reported so far is listed in Table 2. As can be seen, NH_3 yield has not been significantly improved, even with the use of advanced flow electrolytic cells. This motivates improvements in dissolution and mass transfer through electrolyte and electrolytic cell design. Recently, advanced nanoreactor catalysts with confinement function can also promote N transport in the nano space [106,114]. The subsequent adsorption and activation steps are highly dependent on the catalysts.

Table 2. Performance of different flow cells for N_2RR reported.

Type	Catalyst [Ref.]	Electrolyte	NH_3 Formation Rate	Faradaic Efficiency, %	NH_3 Partial Current Density, mA/cm²	Potential, V vs. RHE
Gas diffusion electrode	Fe_2O_3-CNT [134]	$KHCO_3$	2.2×10^{-3} g m^{-2} h^{-1}	~0.025	~0.1	−2.0V vs. Ag/AgCl
	Fe_2O_3-CNT [135]	0.5M KOH	1.06×10^{-11} mol cm^{-2} s^{-1}	0.164	0.34	−2.0V vs. Ag/AgCl
	Fe_2O_3-CNT [136]	0.5M KOH	41.6 μg h^{-1} mg	17.00	<0.05	−0.5
	Fe_2O_3-CNT [137]	0.5M KOH	23.3 μg h^{-1} mg			−0.5
	Fe_2O_3- CNT [138]	0.1M KOH	0.46 μg h^{-1} cm^{-2}	6.04	<0.05	−0.9V vs. Ag/AgCl
	Ru-CNT [139]	0.1M PBS	2.1×10^{-9} mol cm^{-2} s^{-1}	13.5	<0.08	0
	Cu [143]	0.32M KOH		18		−0.3
					0.25	−0.5
microfluidic flow cell	Fe-MoS_2 [133]	0.1 M KCl	97.5 μg h^{-1} cm^{-2}	31.6	0.44	−0.2
	Bi_5O_7I[140]	0.1 M Na_2SO_4	85.45 mg h^{-1} m^{-2}	6.38	<0.05	−0.4

4.3. Adsorption of N_2

The preceding kinetic processes influence N_2 coverage, which is likely the rate-determining step of EN_2F. At low N_2 coverage, the adsorption energy of side reaction feedstocks is greater than that of N_2 (Figure 10A) [131], and H coverage can significantly increase the energy barrier for N_2 activation [144,145]. However, accurately simulating real steady-state conditions, where the molar ratio of N_2 to H_2O is approximately 1:100,000 [115], is challenging, making definitive conclusions difficult.

Following dissolution and mass transfer, N_2 reaches the electrode or catalyst surface and adsorption occurs. To enhance coverage, aerophilic electrode materials have been utilized, with contact angle measurements used to explain the observed phenomena [140,146,147]. Adsorption is divided into physisorption and chemisorption (Figure 11A). In physisorption, there is no electron exchange between N_2 and the catalyst. For catalysts where active sites are directly related to specific surface area, N_2 adsorption-desorption isotherms can be used to assess N_2 physisorption [24,148], especially for layered structures. Suitable surface area and pore structure can expose more adsorption sites, facilitating N_2 mass transfer and

gas diffusion [149,150]. Furthermore, N_2-TPD typically reveals two peaks. The low-temperature peak (below 200 °C) corresponds to N_2 physisorption/desorption, while the high-temperature peak (around 300 °C) represents N_2 chemisorption. The adsorption strength can be inferred by comparing peak position and intensity [103,149]. A linear correlation between NH_3 production and the N_2-TPD peak area has been observed (Figure 11B) [151].

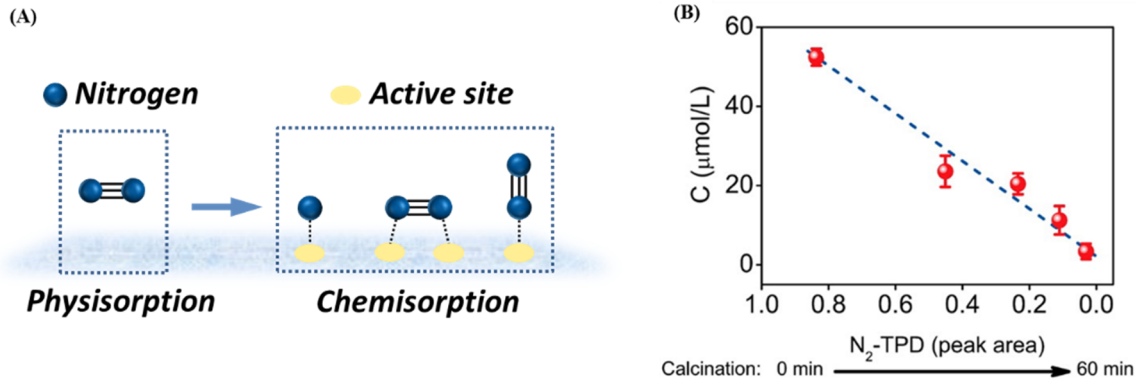

Figure 11. (**A**) Physisorption and three possible chemisorption configurations of N_2. (**B**) Functional relationship between NH_3 yield and the corresponding area of N_2-TPD peak. Reprinted with permission from Ref. [151]. Copyright © 2015, American Chemical Society.

4.4. Activation of N_2

N_2 and the catalyst begin to exchange electrons during chemisorption, also known as N_2 activation. Three possible forms exist (Figure 10A): N_2 dissociation followed by N adsorption, and N_2 adsorption on the catalyst surface via the side or end without bond rupture. Due to its chemical inertness, N_2 chemisorption is difficult. As discussed in the mechanism section, ∗H or ∗OH can facilitate N_2 activation, which is often the RDS for EN_2F. The strong reducing agent Li can react with N_2 at room temperature to generate Li_3N [152–157]. While this strategy is not applicable to N_2OR, identifying a universal nitrogen-fixing active site for EN_2F is more desirable.

4.4.1. Activation Sites of N_2

The essence of chemical reactions lies in the interaction between molecular orbitals. According to the principle of energetic proximity and symmetry matching of frontline orbitals, the HOMO (σ2px) and LUMO (π2py* and π2pz*) of the N_2 molecule can react with d or p orbitals elements. Some transition metals can interfere with the N_2 bonding system through the synergy of occupied and unoccupied d orbitals (Figure 12A) [85]. P-orbital elements are considered potential catalysts for EN_2F due to their unique electronic structure and weak water adsorption. B element of the same period (Figure 12B) and Bi element of the same main group (Figure 12C) as N, both activate N_2 via p orbitals [158,159]. As seen from the energy band diagram (Figure 12C), there is a clear overlap between the Bi6p and N_2p orbitals [140]. A review of Bi for N_2RR has been reported [160]; however, it is worth noting that there is a dispute about Bi catalyzing N_2 [161,162], and in-situ characterization techniques can help resolve this controversy. In addition, nanoscale dual-metal catalysts (Figure 12D) [101] and B-Mo electron transfer pairs (Figure 12E) [110] polarize N_2 in a similar manner. Furthermore, N_2 centered on anion [163,164] or cation [165] vacancies have also been widely studied.

In short, the empty orbitals of the active site coordinated with N_2 consume electrons from the σ2px orbitals of the HOMO level of N, while the occupied orbitals feedback electrons to the π2p* antibonding orbitals of the LUMO level via the "Acceptance and backdonation mechanism". By regulating the surface electronic structure of the heterogeneous catalyst, the more electrons fill the π2p* antibonding orbitals, the easier the N≡N bond is activated and broken [133]. The feedback π bond enhances the bonding of the catalyst and the nitrogen atom, where charge distribution is variational, creating significant imbalance in the band alignment to polarize N_2 and elongate the bond length of N≡N, weakening N_2 bond energy for further reaction.

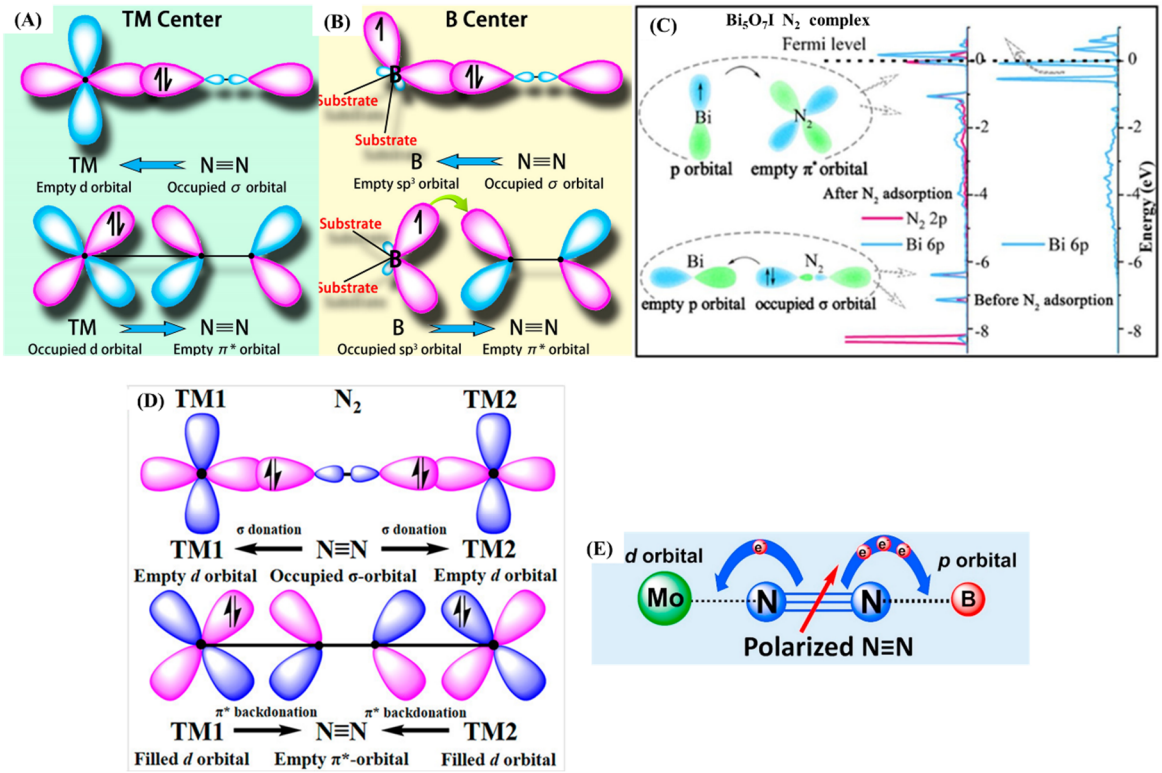

Figure 12. Simplified schematic of N_2 bonding to (**A**) transition metal; (**B**) boron; (**C**) bismuth; (**D**) dual-metal; and (**E**) B-Mo pair. Reprinted with permission from Ref. [101,159]. Copyright © 2018, 2020, American Chemical Society. Reprinted with permission from Ref. [140]. Copyright © 2020, Elsevier.

4.2.2. Characterization of N_2 Activation

Directly characterizing the chemisorption of N_2 and reaction intermediates on the catalyst surface is challenging, but some in-situ characterization techniques are helpful. The in-situ near-environmental pressure XPS technique was used by Han's group to detect active sites on FeMo/NC, where Fe atoms gained electrons from N_2 and the valence band decreased, while Mo atoms donated electrons whose valence band rose [105]. Peng tested a monoatomic catalyst at different voltages by in-situ XAS and found the change of oxidation state of monoatomic Ru upon activation of N_2, proving that Ru was the active center [166]. Yao attempted to explain the controversial Bi activity by in-situ Raman under a long voltage window (−1.1 V ~ 0.1 V). The authors inferred that during electrochemical reduction, Bi-MOF nanorods underwent significant structural rearrangement and chemical transformation to Bi, and in-situ reduced 0-valent metallic Bi was the predominant active species for N_2RR [167]. Liu used in-situ XRD and in-situ Raman to detect the appearance of B-N bonds after electrochemical activation on B-rich COFs, demonstrating that non-metallic B was the activation site [168]. Li calculated the rate constants of the main and side reactions by in-situ scanning electrochemical microscopy, which proved the high selectivity of the catalyst to N_2 activation [114].

To clearly understand the reaction mechanism, real-time direct electrochemical mass spectrometry analysis of the evolved gas was performed under various applied potentials and concluded that N_2RR would not form a stable end-product hydrazine [169,170]. Yao used in-situ surface-enhanced infrared spectroscopy to examine the surfaces of a series of noble metals (e.g., Au, Pt, Rh, and Ru) and detected that the reaction intermediate $*N_2H_x$ had different pathways and elucidated the relationship between voltage and the side reaction [171–173]. Lv and Qu respectively used in-situ Fourier transform infrared spectroscopy to prove that non-noble metals followed the associative pathway [24,174].

To test the stability of the catalyst, Yang confirmed the active phase of the N_2 reaction using in-situ XAS and found that the catalyst underwent a phase change leading to performance degradation [175]. Luo used in-situ electrochemical quartz-crystal microbalance to study the variation in catalyst quality, revealing that O vacancies as active sites were likely to be filled, and calling for elaborative examination of the stability of catalysts that vacancies were the active sites [176]. EN_2F must go through the initial kinetic steps of N_2 dissolution, mass transfer, adsorption, and activation in sequence. Based on the existing literature, this chapter introduces general improvement and characterization methods for these steps in three aspects: electrolyte,

electrolytic cell, and catalyst. The current literature is dominated by N_2RR, but the organized methods are also suitable for N_2OR and are still far from adequate, requiring more attempts and validations by scientists.

5. Selectivity and Improvement

Although the secondary reaction intermediate (H^+ or OH^-) bonded to N is beneficial for N_2 activation, uncontrolled, it will surpass the main reaction. Limiting the side reaction is mentioned in almost every article, and increasing selectivity is the current focus of EN_2F, with specific reviews [85,177], viewpoints [117], and perspectives [178] discussing or addressing the issue of selectivity.

In experiments, the electrochemical properties of primary and secondary reactions can be tested separately to compare and judge the reaction selectivity and activity, and the optimal potential interval can be explored. Slight current differences can be seen in polarization or cyclic voltammetry tests under N_2 and Ar atmospheres [68,92]. The activation energy of the main and side reactions can also be calculated by the Arrhenius equation, where a smaller activation energy means higher selectivity [130]. Most articles that include theoretical calculations use ΔG_{N2RR}-ΔG_{HER} as the descriptor for N_2RR selectivity determination (ΔG_{N2RR}, ΔG_{HER} are the free energy required for the reaction) [133,179,180]. It was found from the volcano map that the potential limit of HER is lower, so it is kinetically more likely to occur, reflecting the difficulty of N_2RR. Also if the volcano curve is separated at ΔG_N, indicating a higher selectivity of the catalyst [178].

To improve the selectivity and activity of EN_2F, it is crucial to optimize the composition of the inner Helmholtz plane of the working electrode to limit the transport and utilization of protons in N_2RR and hydroxyl groups in N_2OR (Figure 13) [117]. Relevant specific measures related to the latest report are provided below.

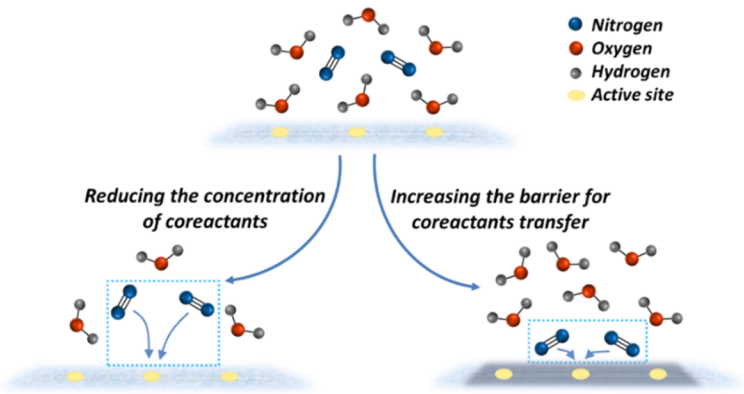

Figure 13. Two common strategies to improve selectivity of EN_2F.

5.1. Reducing the Concentration of Core Actants

5.1.1. PH

The proton concentration in aqueous solution affects N coverage at the active sites for N_2RR. Using alkaline solvents to reduce the number of protons can thermodynamically impede proton transfer [117]. N_2RR has been reported to be more productive and efficient in neutral or alkaline solutions. For instance, 0.1M KOH [181], 0.1M Li_2SO_4 [182], or 0.1M PBS [89] were chosen as electrolytes by directly comparing the electrochemical performance of different pH electrolytes. More precisely, Zhang's group detected the ammonia yield of 10 electrolytes by ion chromatography and ultimately chose neutral 0.1 M KCl as the optimal electrolyte. For N_2OR, experimenting under neutral pH has two advantages for improving selectivity: it averts excessive OH^- coverage and the resulting side reaction, and it avoids the coincidence of voltage under acidic conditions (pH = 1.3) bringing a wide voltage window [34]. Note that while a strong alkaline electrolyte may provide high performance, the corrosiveness of the electrolyte often causes electrocatalyst failure.

5.1.2. Alkali Metal Ions

The hydrated ions formed by alkali metal cations and H_2O in the electrolyte migrate to the electrode-electrolyte interface under the electric field, affecting the local electric field strength and pH [183], which has

a strong correlation with the selectivity of the catalytic reaction. They also have a certain effect on the side reactions HER [184,185] and OER [186,187]. Guha and Narayanan combined experiments and theoretical calculations to study in detail the role of Li+ in stabilizing nitrogen near the working electrode [188]. When Cu and Au were used as working electrodes, the yield and selectivity both increased with the rise of the concentration of $LiClO_4$ (from 0.1M to 5M). XPS analysis indicated that the effect of Li+ was transient. DFT calculations revealed that Li^+ not only adsorbed N_2 but also helped dissociate the N≡N triple bond [189]. Hao and Yin found that K^+ increased the yields and selectivities of Bi, Au, and Pt, all of which were directly related to K^+ concentration (0.2M to 1M). From the experimental data, it was speculated that the inhibitory effect of K^+ on HER was attributed to the blocked migration of protons from the native solution to the electrode surface [190]. Kani also found K^+ with the highest FE for N_2RR from Li^+ to Rb^+ [143]. While, Rondinone drew a conclusion that Li^+ was the best cation enhancing the electric field by comparing the influence of Li^+, Na^+, K^+ on the thickness of the electric double layer. The electric field at the tip of the catalyst surface increased as the reduced size of the cation and the formation of dehydrated cation layer inhibited the migration of protons [191]. The performance of EN_2F can be improved by adjusting the alkali metal cations.

5.1.3 Aprotic Solvents

Aprotic solvents were introduced to control the concentration of protons in the electrolyte. Thermodynamic evaluation in organic acetonitrile solution shows that N_2RR is preferred compared to H^+ reduction [192]. Zhang and Nørskov found through theoretical calculations that 2,6-lutidinium was a feasible alternative to hydronium ion, which could break the linear relationship and stabilize the ∗NNH intermediate. The Volmer reaction using 2,6-lutidinium required high energy barrier was suppressed, compared with H_3O^+ [193]. Over time, experimental studies of other solvents included alcohol + acid [194,195], ethylenediamine + acid [196], polymer gel + water [197], tetrahydrofuran + alcohol [180,198,199], ionic liquid + water [118,120,121] etc., that mixed with trace amounts of proton sources to limit protons and improve selectivity [117], in which ionic liquids have been reported in detail in the N_2 dissolution section.

5.2. Increasing the Barrier for Core Actants Transfer

5.2.1. Protective Layer

Covering the catalyst surface with a hydrophobic protective layer can lower the coverage and interaction of H_2O, kinetically increasing the barrier for core actants transfer [117]. Ling's group did some meaningful researches [180,198,199]. In a recent study, the FE of the electrocatalyst Pt/Au@ZIF coated with ZIF as a hydrophobic layer was much greater than that of the uncoated Pt/Au. The coating layer had three functions: it modified the d-band structure of Pt/Au to weaken the adsorption of H, induced Pt as an active site to strengthen the affinity of N_2, and repelled humidity to inhibit side reactions [180]. In another advanced study, a hydrophobic oleyl amine-functionalized ZIF was used as a coating layer, and butanol was added as a molecular filler in the pores to further block water molecules and change water from obstacle to accelerator and proton source [198]. Yang also inhibited the side reaction by ZIF coating [200]. In addition to using MOFs, Zheng and Liu constructed hybrid electrodes for EN_2F using hydrophobic PTFE [146] and carbon spheres [140] as protective layers, respectively.

5.2.2. Cell Design

In particular, it was mentioned above that Chen increased the efficiency of ammonia production by increasing the transport path to slow down the rate at which protons reached the active site through an additional gas diffusion layer in a flow cell [135–137]. Liu controlled the transfer rate of H^+ by adjusting the pore area of a polypropylene membrane in an H-type cell and used a physical model to reveal and predict the trend of FE [107]. Thus, it can be seen that the newfangled design of electrolytic cells can also improve the selectivity of EN_2F [126].

5.3. Limiting the Electrons Transfer

The third common solution is restricting electronics [117]. Chen's group tested the Cu-2 electrode using electrochemical impedance spectroscopy and found an increase in charge transfer resistance, who claimed that limiting the utilization of electrons improved the performance of N_2RR because the determining factor of HER was the electron transfer step, while the RDS of N_2RR was the coverage of N_2 on the catalyst surface [201]. The current methods to improve the selectivity of N_2RR mainly focus on the

control of the number and transport of protons. Limiting electrons to improve selectivity is equivalent to increasing the resistance of the electrochemical reaction system, which is not conducive to the primary reaction. It should also be noted that both the main reaction and the side reaction of N_2OR lose 4 electrons, so limiting electrons does not seem to be appropriate for N_2OR.

The current scientific community have significantly increased FEs, but often accompanied with very low yields [131], which means that overly restricting the secondary reactions goes against the activities of EN_2F [36]. Not surprisingly, the above discussion of selectivity also focuses on the three components of the electrolyte, electrolytic cell, and catalyst [177]. Although a widely agreed universal experimental approach has not yet been developed, the above strategies, which are highly instructive in terms of experimental direction, are applicable to both N_2RR and N_2OR except for the third one. Based on these strategies, more specific and novel methods need to be further expanded and verified.

6. Summary and Prospect

6.1. Summary

This review provides a parallel and integrative analysis of cathodic N_2 reduction and anodic N_2 oxidation within a unified kinetic and mechanistic framework for electrochemical nitrogen fixation (EN_2F). By systematically comparing reaction mechanisms, competing side reactions, and kinetic constraints across both pathways, common challenges and transferable design principles are identified, offering a coherent perspective that bridges traditionally separated research directions.

(1) Regarding reaction mechanisms, N_2RR features well-defined pathways, with a focus shifting from N_2 adsorption and activation to H dissociation. In contrast, the N_2OR mechanism remains unclear, with ongoing debate between O-preferred and N-preferred pathways.

(2) Both EN_2F processes suffer from selectivity issues due to the competitive water splitting reaction. While unavoidable, these competitive reactions can promote N_2 activation and enhance EN_2F activity.

(3) Both EN_2F reactions share common kinetic steps (N_2 dissolution, diffusion, adsorption, and activation) and face challenges related to selectivity and AN pollution. Addressing these issues can benefit from mutual learning and collaborative development.

(4) Both are constrained by traditional scaling relationships, and strategies to overcome these limitations can be mutually beneficial. Both have seen the development of new catalysts utilizing competitive reactions. Furthermore, advances in in-situ characterization techniques and theoretical calculations will accelerate the progress of EN_2F.

6.2. Prospect

6.2.1. Experimental Details

When nitrogen exists in the oxidized state (various oxides or acids of nitrogen) or reduced state (NH_3 or N_2H_4), it can be called the active state of nitrogen (AN). Even commercial nitrogen-free metal oxides contain AN [202]. Many reported literatures have false positive results, where AN is the real raw material rather than N_2 [203]. There are many experimental benchmarks and protocols for N_2RR [33], which are also applicable to N_2OR. Here, they are concisely organized into the following points: (1) Pretreatment of raw materials: The treatment methods of feed gas N_2 applied in different scenarios were listed in detail in the perspective [204]. The membrane needs to be washed with acid and H_2O_2 several times before using, which is a critical step [129]. In addition, studies have shown that the use of a polypropylene membrane can avoid AN pollution caused by Nafion film [130]. (2) Judgment of AN pollution: A sealed cell and two detection methods must be used to test the yield accurately. Ar atmosphere, open circuit voltage, and blank experiment without catalyst must be conducted one by one before the experiment to obtain the corresponding data of AN pollution, confirming whether it is in the reasonable range. (3) Yield calculation: The result is the yield under catalytic conditions minus that of AN pollution. (4) Long cycle experiment: Calculate whether the final yield increases linearly with time under N_2 atmosphere; if not, it means that the yield comes from AN pollution, which is gradually consumed with the reaction. A long N_2 cycle is also helpful to judge the stability of the catalyst. (5) Using an Ar/N_2 alternating cycle test, the alternating change of yield shows that N_2 is reacting. Strict N_2 isotope control is important, especially for experiments with catalysts or electrolytes containing element N.

6.2.2. Improvement

Due to the ubiquitous AN pollution and difficulty improving the yield, the EN_2F field seems to be entering a bottleneck period. To pursue relatively high yield and selectivity, most studies focus on catalysts. (1) Regardless of how catalysts are regulated, performance may not improve significantly, suggesting that the rate-determining step of EN_2F may be N_2 coverage. Improving the solubility and transfer of N_2, which has been proven to enhance the performance of EN_2F, has a lot of room for expansion. (2) Focus should continue to be on how to eliminate and quantify pollution, which is vital to the healthy development of the area. (3) More attention should be paid to how side reactions promote the activation of N_2 during the catalysis process. Thinking about how to exceed the scaling relationships, the research on the active site and the carrier needs to be more in-depth. Promoters in catalysts have the function of avoiding the relationship [205], but there is no research on it in the electrocatalytic reaction. (4) The computational supporting information in some experimental articles is not accurate enough. For example, some of the accompanying DFT calculations show that the thermodynamic barrier of the process is about 2eV, which results in a turnover rate of about 10^{-16} s^{-1} [206]. Since the experimental benchmark has been mentioned many times, are there any calculation or combinations of calculation and experiment protocols, which should be done by more seasoned and experienced theoretical computational scientists.

6.2.3. Thermochemistry

In the table of thermodynamic parameters (Table 3), the energy requirements for plasma-driven N_2 and O_2 reactions (reactions 1–4) are significantly lower than those for N_2OR (reaction 7) and N_2RR (reaction 11), highlighting the advantage of plasma processes. With the exception of the HB reaction 8, all reactions using N_2 as a raw material are endothermic. In most cases, the energy requirements per electron (applied voltage V) are quite low; specifically, the applied voltage for nitrogen oxidation reactions (reactions 1–7) is notably lower than that for N_2RR (reactions 9–11), demonstrating an advantage for N_2OR [207]. When water serves as the reducing agent or oxidant, the energy demand is comparable between N_2RR reactions 9–11 and N_2OR reaction 7. However, given that the solubility of oxygen is approximately twice that of nitrogen (Figure 10A), the addition of O_2 during the oxidation reaction (or coupling anode N_2OR and cathode ORR, cell 2 in Table 4) results in a higher oxidation capacity compared to H_2O. Consequently, the energy for reaction 6 is 89.26 kJ/mol N_2, only 1/7 of that for N_2RR reaction 11, significantly reducing the overall energy requirement. In N_2OR experiments, the source of nitrogen oxidation (O_2 or H_2O) remains uncertain. Therefore, employing corresponding O isotope experiments can help resolve this ambiguity. The first nitrogen fixation process for industrial application was the plasma-driven N_2 oxidation process (Birkeland-Eyde process) in 1903. The Haber-Bosch process gained industrial dominance in 1913 [208]. With the emergence of EN_2F, projected to increase gradually until 2040 [16], competition among various technical routes will persist. Ultimately, determining the likelihood of N_2RR or N_2OR requires more thermodynamic data, process simulation, and experimental exploration.

Table 3. Thermodynamic parameters of N_2 oxidation and reduction reactions under standard conditions. Data are sourced from the NIST Standard Reference Database [209]. Parameters include the number of electrons transferred (n_e), voltage per electron (ΔV), and change in nitrogen redox state (ΔeN).

Classification	Rank	Reaction	ΔG, kJ/mol N_2	n_e	ΔV, V	Δe_N
Nitrogen Oxidation	1	$N_2(g) + O_2(g) = 2NO(g)$	173.2	4	0.45	2
	2	$N_2(g) + 3/2O_2(g) = 2N_2O_3(g)$	139.73	6	0.24	3
	3	$N_2(g) + 2O_2(g) = 2NO_2(g)$	102.52	8	0.13	4
	4	$N_2(g) + 5/2O_2(g) = N_2O_5(g)$	118.01	10	0.12	5
	5	$N_2(g) + H_2O(l) + 3/2O_2(g) = 2HNO_2(g)$	153.36	6	0.27	3
	6	$N_2(g) + H_2O(l) + 5/2O_2(g) = 2HNO_3(g)$	89.26	10	0.093	5
	7	$N_2(g) + 2H_2O(l) = 2NO(g) + 2H_2(g)$	447.48	4	1.16	2
Nitrogen Reduction	8	$N_2(g) + 3H_2(g) = 2NH_3(g)$	−32.73	6	−0.057	−3
	9	$N_2(g) + H_2O(l) = N_2H_2(g) + 1/2O_2(g)$	481.02	2	2.5	−1
	10	$N_2(g) + 2H_2O(l) = N_2H_4(g) + O_2(g)$	633.51	4	1.65	−2
	11	$N_2(g) + 3H_2O(l) = 2NH_3(g) + 3/2O_2(g)$	678.69	6	1.18	−3

Table 4. Full cell configurations combining EN_2F with other half-reactions.

	Cathode	Anode	Full Cell
Cell 1	N_2RR: $N_2 + 6H^+ + 6e^- = 2NH_3$	OER: $2H_2O - 4e^- = O_2 + 4H^+$	$2N_2 + 6H_2O = 4NH_3 + 3O_2$
Cell 2	ORR: $O_2 + 4H^+ + 4e^- = 2H_2O$	N_2OR: $N_2 + 6H_2O - 10e^- = 2HNO_3 + 10H^+$	$2N_2 + 5O_2 + 2H_2O = 4HNO_3$
Cell 3	HER: $2H + 2e^- = H_2$	N_2OR: $N_2 + 6H_2O - 10e^- = 2HNO_3 + 10H^+$	$N_2 + 6H_2O = 2HNO_3 + 5H_2$
Cell 4	N_2RR: $N_2 + 6H^+ + 6e^- = 2NH_3$	N_2OR: $N_2 + 6H_2O - 10e^- = 2HNO_3 + 10H^+$	$4N_2 + 9H_2O = 2NH_3 + 3NH_4NO_3$

6.2.4. Full cell reactions

Electricity is poised to become the dominant energy source in the future. The integration of EN_2F with other half-reactions (HER, ORR, OER) to form complete cells (Table 4) holds significant application potential. Cell 1 and Cell 3 represent current research focuses for N_2RR and N_2OR, respectively. Cell 2, as discussed in Section 6.1.3, offers the benefit of reduced reaction energy and maximized atomic utilization. The development of Cell 4 could enable direct synthesis of ammonium nitrate for agricultural production from EN_2F under mild conditions.

Author Contributions

X.M.: conceptualization, methodology, data curation, writing—original draft preparation, visualization, investigation; X.W.: conceptualization, methodology; J.L.: conceptualization, methodology; Y.M.: conceptualization, methodology, supervision, writing—reviewing and editing. All authors have read and agreed to the published version of the manuscript.

Funding

The authors acknowledge the support from the Basic Research Program of Liaoning Provincial Universities (LJ212510146030), University of Science and Technology Liaoning (USTL) and RMIT University.

Data Availability Statement

The data are available from the corresponding author upon reasonable request.

Conflicts of Interest

The authors declare no conflict of interest.

Use of AI and AI-Assisted Technologies

No AI tools were utilized for this paper.

References

1. Ye, L.; Nayak-Luke, R.; Bañares-Alcántara, R.; et al. Reaction: "Green" Ammonia Production. *Chem* **2017**, *3*, 712–714. https://doi.org/10.1016/j.chempr.2017.10.016.
2. Heffer, P.; Prud'homme, M. Global Nitrogen Fertiliser Demand and Supply Trend, Current Level and Outlook. In Proceedings of the 2016 International Nitrogen Initiative Conference, "Solutions to Improve Nitrogen Use Efficiency for the World", Melbourne, VIC, Australia, 4–8 December 2016.
3. Smil, V. Detonator of the Population Explosion. *Nature* **1999**, *400*, 415. https://doi.org/10.1038/22672.
4. Yu, Y.-H.; Yuan, Y.-F.; Li, W.; et al. Unveiling Cutting-Edge Developments on d-Block Iron-Based Materials for Electrocatalytic Ammonia Synthesis. *Rare Met.* **2025**, *44*, 9785–9798. https://doi.org/10.1007/s12598-025-03592-5.
5. Guo, J.; Chen, P. Catalyst: NH_3 as an Energy Carrier. *Chem* **2017**, *3*, 709–712. https://doi.org/10.1016/j.chempr.2017.10.004.
6. Giddey, S.; Badwal, S.P.S.; Munnings, C.; et al. Ammonia as a Renewable Energy Transportation Media. *ACS Sustain. Chem. Eng.* **2017**, *5*, 10231–10239. https://doi.org/10.1021/acssuschemeng.7b02219.
7. Li, R.; Bao, L.; Li, J.; et al. Construction of Multiple Active Sites for Energy-Efficient Ammonia Production by Nitrate Reduction Coupling with Urea Oxidation. *Chem. Eng. J.* **2025**, *524*, 169332. https://doi.org/10.1016/j.cej.2025.169332.
8. Groves, M.C.E. Nitric Acid. In *Kirk-Othmer Encyclopedia of Chemical Technology*; John Wiley & Sons: Hoboken, NJ, USA, 2020; pp. 1–37.
9. Yu, Y.; Li, J.; Yue, Z.; et al. Advances in Multiple Active Site Catalysts for Urea Synthesis via Electrocatalytic C–N Coupling. *Trans. Tianjin Univ.* **2025**, *31*, 478–497. https://doi.org/10.1007/s12209-025-00444-2.

10. Kyriakou, V.; Garagounis, I.; Vourros, A.; et al. An Electrochemical Haber-Bosch Process. *Joule* **2020**, *4*, 142–158. https://doi.org/10.1016/j.joule.2019.10.006.
11. Jiang, L.; Liu, F. Carbon Dioxide and Nitrate Electrocatalytic C–N Coupling for Sustainable Production of Urea. *Sci. Energy Environ.* **2024**, *1*, 2. https://doi.org/10.53941/see.2024.100002.
12. Smith, C.; Hill, A.K.; Torrente-Murciano, L. Current and Future Role of Haber-Bosch Ammonia in a Carbon-Free Energy Landscape. *Energy Environ. Sci.* **2020**, *13*, 331–344. https://doi.org/10.1039/c9ee02873k.
13. Wang, Q.; Guo, J.; Chen, P. Recent Progress Towards Mild-Condition Ammonia Synthesis. *J. Energy Chem.* **2019**, *36*, 25–36. https://doi.org/10.1016/j.jechem.2019.01.027.
14. Pérez-Ramírez, J.; Kapteijn, F.; Schöffel, K.; et al. Formation and Control of N_2O in Nitric Acid Production. *Appl. Catal. B* **2003**, *44*, 117–151. https://doi.org/10.1016/s0926-3373(03)00026-2.
15. Schiffer, Z.J.; Manthiram, K. Electrification and Decarbonization of the Chemical Industry. *Joule* **2017**, *1*, 10–14. https://doi.org/10.1016/j.joule.2017.07.008.
16. MacFarlane, D.R.; Cherepanov, P.V.; Choi, J.; et al. A Roadmap to the Ammonia Economy. *Joule* **2020**, *4*, 1186–1205. https://doi.org/10.1016/j.joule.2020.04.004.
17. Stevens, C.J. Nitrogen in the Environment. *Science* **2019**, *363*, 578–580. https://doi.org/10.1126/science.aav8215.
18. Chen, J.G.; Crooks, R.M.; Seefeldt, L.C.; et al. Beyond Fossil Fuel-Driven Nitrogen Transformations. *Science* **2018**, *360*, 873–880. https://doi.org/10.1126/science.aar6611.
19. Cui, X.; Tang, C.; Zhang, Q. A Review of Electrocatalytic Reduction of Dinitrogen to Ammonia under Ambient Conditions. *Adv. Energy Mater.* **2018**, *8*, 1800369–1800394. https://doi.org/10.1002/aenm.201800369.
20. Soloveichik, G. Electrochemical Synthesis of Ammonia as a Potential Alternative to the Haber-Bosch Process. *Nat. Catal.* **2019**, *2*, 377–380. https://doi.org/10.1038/s41929-019-0280-0.
21. Qing, G.; Ghazfar, R.; Jackowski, S.T.; et al. Recent Advances and Challenges of Electrocatalytic N_2 Reduction to Ammonia. *Chem. Rev.* **2020**, *120*, 5437–5516. https://doi.org/10.1021/acs.chemrev.9b00659.
22. Yang, C.; Zhu, Y.; Liu, J.; et al. Defect Engineering for Electrochemical Nitrogen Reduction Reaction to Ammonia. *Nano Energy* **2020**, *77*, 105126. https://doi.org/10.1016/j.nanoen.2020.105126.
23. Liu, J.; Wang, G.; Zhou, S.; et al. CeO_2-Supported Monodispersed MoO_3 Clusters for High-Efficiency Electrochemical Nitrogen Reduction under Ambient Condition. *J. Energy Chem.* **2021**, *56*, 186–192. https://doi.org/10.1016/j.jechem.2020.07.042.
24. Lv, X.-W.; Liu, Y.; Wang, Y.-S.; et al. Encapsulating Vanadium Nitride Nanodots into N,S-Codoped Graphitized Carbon for Synergistic Electrocatalytic Nitrogen Reduction and Aqueous Zn-N_2 Battery. *Appl. Catal. B* **2021**, *280*, 119434–119442. https://doi.org/10.1016/j.apcatb.2020.119434.
25. Wang, Y.; Yu, Y.; Jia, R.; et al. Electrochemical Synthesis of Nitric Acid from Air and Ammonia through Waste Utilization. *Natl. Sci. Rev.* **2019**, *6*, 730–738. https://doi.org/10.1093/nsr/nwz019.
26. Peng, X.; Mi, Y.; Bao, H.; et al. Ambient Electrosynthesis of Ammonia with Efficient Denitration. *Nano Energy* **2020**, *78*, 105321. https://doi.org/10.1016/j.nanoen.2020.105321.
27. Long, J.; Chen, S.; Zhang, Y.; et al. Direct Electrochemical Ammonia Synthesis from Nitric Oxide. *Angew. Chem. Int. Ed.* **2020**, *59*, 9711–9718. https://doi.org/10.1002/anie.202002337.
28. Li, J.; Zhan, G.; Yang, J.; et al. Efficient Ammonia Electrosynthesis from Nitrate on Strained Ruthenium Nanoclusters. *J. Am. Chem. Soc.* **2020**, *142*, 7036–7046. https://doi.org/10.1021/jacs.0c00418.
29. Chen, G.-F.; Yuan, Y.; Jiang, H.; et al. Electrochemical Reduction of Nitrate to Ammonia via Direct Eight-Electron Transfer Using a Copper–Molecular Solid Catalyst. *Nat. Energy* **2020**, *5*, 605–613. https://doi.org/10.1038/s41560-020-0654-1.
30. Wang, Y.; Zhou, W.; Jia, R.; et al. Unveiling the Activity Origin of a Copper-Based Electrocatalyst for Selective Nitrate Reduction to Ammonia. *Angew. Chem. Int. Ed.* **2020**, *59*, 5350–5354. https://doi.org/10.1002/anie.201915992.
31. Rod, T.H.; Logadottir, A.; Nørskov, J.K. Ammonia Synthesis at Low Temperatures. *J. Chem. Phys.* **2000**, *112*, 5343–5347. https://doi.org/10.1063/1.481103.
32. van der Ham, C.J.; Koper, M.T.; Hetterscheid, D.G. Challenges in Reduction of Dinitrogen by Proton and Electron Transfer. *Chem. Soc. Rev.* **2014**, *43*, 5183–5191. https://doi.org/10.1039/c4cs00085d.
33. Tang, C.; Qiao, S.Z. How to Explore Ambient Electrocatalytic Nitrogen Reduction Reliably and Insightfully. *Chem. Soc. Rev.* **2019**, *48*, 3166–3180. https://doi.org/10.1039/c9cs00280d.
34. Fang, W.; Du, C.; Kuang, M.; et al. Boosting Efficient Ambient Nitrogen Oxidation by a Well-Dispersed Pd on MXene Electrocatalyst. *Chem. Commun.* **2020**, *56*, 5779–5782. https://doi.org/10.1039/d0cc01759k.
35. Koper, M.T.M. Theory of Multiple Proton-Electron Transfer Reactions and Its Implications for Electrocatalysis. *Chem. Sci.* **2013**, *4*, 2710–2723. https://doi.org/10.1039/c3sc50205h.
36. Cheng, H.; Ding, L.X.; Chen, G.F.; et al. Molybdenum Carbide Nanodots Enable Efficient Electrocatalytic Nitrogen Fixation under Ambient Conditions. *Adv. Mater.* **2018**, *30*, 1803694. https://doi.org/10.1002/adma.201803694.

37. Honkala, K.; Hellman, A.; Remediakis, I.N.; et al. Ammonia Synthesis from First-Principles Calculations. *Science* **2005**, *307*, 555–558. https://doi.org/10.1126/science.1106435.
38. Montoya, J.H.; Tsai, C.; Vojvodic, A.; et al. The Challenge of Electrochemical Ammonia Synthesis: A New Perspective on the Role of Nitrogen Scaling Relations. *ChemSusChem* **2015**, *8*, 2180–2186. https://doi.org/10.1002/cssc.201500322.
39. Garden, A.L.; Skúlason, E. The Mechanism of Industrial Ammonia Synthesis Revisited: Calculations of the Role of the Associative Mechanism. *J. Phys. Chem. C* **2015**, *119*, 26554–26559. https://doi.org/10.1021/acs.jpcc.5b08508.
40. Singh, A.R.; Montoya, J.H.; Rohr, B.A.; et al. Computational Design of Active Site Structures with Improved Transition-State Scaling for Ammonia Synthesis. *ACS Catal.* **2018**, *8*, 4017–4024. https://doi.org/10.1021/acscatal.8b00106.
41. Kitano, M.; Kanbara, S.; Inoue, Y.; et al. Electride Support Boosts Nitrogen Dissociation over Ruthenium Catalyst and Shifts the Bottleneck in Ammonia Synthesis. *Nat. Commun.* **2015**, *6*, 6731–6740. https://doi.org/10.1038/ncomms7731.
42. Song, T.; Hu, P. Insight into the Adsorption Competition and the Relationship between Dissociation and Association Reactions in Ammonia Synthesis. *J. Chem. Phys.* **2007**, *127*, 234706–234715. https://doi.org/10.1063/1.2799984.
43. Buscagan, T.M.; Rees, D.C. Rethinking the Nitrogenase Mechanism: Activating the Active Site. *Joule* **2019**, *3*, 2662–2678. https://doi.org/10.1016/j.joule.2019.09.004.
44. Kobayashi, Y.; Kitano, M.; Kawamura, S.; et al. Kinetic Evidence: The Rate-Determining Step for Ammonia Synthesis over Electride-Supported Ru Catalysts Is No Longer the Nitrogen Dissociation Step. *Catal. Sci. Technol.* **2017**, *7*, 47–50. https://doi.org/10.1039/c6cy01962e.
45. Matsuishi, S.; Toda, Y.; Miyakawa, M.; et al. High-Density Electron Anions in a Nanoporous Single Crystal: $[Ca_{24}Al_{28}O_{64}]^{4+}(4e^-)$. *Science* **2003**, *301*, 626–629. https://doi.org/10.1126/science.1083842.
46. Kitano, M.; Inoue, Y.; Yamazaki, Y.; et al. Ammonia Synthesis Using a Stable Electride as an Electron Donor and Reversible Hydrogen Store. *Nat. Chem.* **2012**, *4*, 934–940. https://doi.org/10.1038/nchem.1476.
47. Kanbara, S.; Kitano, M.; Inoue, Y.; et al. Mechanism Switching of Ammonia Synthesis Over Ru-Loaded Electride Catalyst at Metal-Insulator Transition. *J. Am. Chem. Soc.* **2015**, *137*, 14517–14524. https://doi.org/10.1021/jacs.5b10145.
48. Kitano, M.; Inoue, Y.; Ishikawa, H.; et al. Essential Role of Hydride Ion in Ruthenium-Based Ammonia Synthesis Catalysts. *Chem. Sci.* **2016**, *7*, 4036–4043. https://doi.org/10.1039/c6sc00767h.
49. Wu, J.; Gong, Y.; Inoshita, T.; et al. Tiered Electron Anions in Multiple Voids of LaScSi and Their Applications to Ammonia Synthesis. *Adv. Mater.* **2017**, *29*, 1700924–1700931. https://doi.org/10.1002/adma.201700924.
50. Wu, J.; Li, J.; Gong, Y.; et al. Intermetallic Electride Catalyst as a Platform for Ammonia Synthesis. *Angew. Chem. Int. Ed.* **2019**, *58*, 825–829. https://doi.org/10.1002/anie.201812131.
51. Hattori, M.; Mori, T.; Arai, T.; et al. Enhanced Catalytic Ammonia Synthesis with Transformed BaO. *ACS Catal.* **2018**, *8*, 10977–10984. https://doi.org/10.1021/acscatal.8b02839.
52. Nakao, T.; Tada, T.; Hosono, H. Transition Metal-Doped Ru Nanoparticles Loaded on Metal Hydrides for Efficient Ammonia Synthesis from First Principles. *J. Phys. Chem. C* **2019**, *124*, 1529–1534. https://doi.org/10.1021/acs.jpcc.9b10544.
53. Kitano, M.; Kujirai, J.; Ogasawara, K.; et al. Low-Temperature Synthesis of Perovskite Oxynitride-Hydrides as Ammonia Synthesis Catalysts. *J. Am. Chem. Soc.* **2019**, *141*, 20344–20353. https://doi.org/10.1021/jacs.9b10726.
54. Hattori, M.; Iijima, S.; Nakao, T.; et al. Solid Solution for Catalytic Ammonia Synthesis from Nitrogen and Hydrogen Gases at 50 °C. *Nat. Commun.* **2020**, *11*, 2001–2009. https://doi.org/10.1038/s41467-020-15868-8.
55. Ye, T.N.; Park, S.W.; Lu, Y.; et al. Vacancy-Enabled N_2 Activation for Ammonia Synthesis on an Ni-Loaded Catalyst. *Nature* **2020**, *583*, 391–395. https://doi.org/10.1038/s41586-020-2464-9.
56. Ma, X.L.; Liu, J.C.; Xiao, H.; et al. Surface Single-Cluster Catalyst for N_2-to-NH_3 Thermal Conversion. *J. Am. Chem. Soc.* **2018**, *140*, 46–49. https://doi.org/10.1021/jacs.7b10354.
57. Liu, J.C.; Ma, X.L.; Li, Y.; et al. Heterogeneous Fe_3 Single-Cluster Catalyst for Ammonia Synthesis via an Associative Mechanism. *Nat. Commun.* **2018**, *9*, 1610–1619. https://doi.org/10.1038/s41467-018-03795-8.
58. Rostamikia, G.; Maheshwari, S.; Janik, M.J. Elementary Kinetics of Nitrogen Electroreduction to Ammonia on Late Transition Metals. *Catal. Sci. Technol.* **2019**, *9*, 174–181. https://doi.org/10.1039/c8cy01845f.
59. Jasniewski, A.J.; Lee, C.C.; Ribbe, M.W.; et al. Reactivity, Mechanism, and Assembly of the Alternative Nitrogenases. *Chem. Rev.* **2020**, *120*, 5107–5157. https://doi.org/10.1021/acs.chemrev.9b00704.
60. Cao, L.; Ryde, U. Putative Reaction Mechanism of Nitrogenase after Dissociation of a Sulfide Ligand. *J. Catal.* **2020**, *391*, 247–259. https://doi.org/10.1016/j.jcat.2020.08.028.
61. Zhao, J.; Chen, Z. Single Mo Atom Supported on Defective Boron Nitride Monolayer as an Efficient Electrocatalyst for Nitrogen Fixation: A Computational Study. *J. Am. Chem. Soc.* **2017**, *139*, 12480–12487. https://doi.org/10.1021/jacs.7b05213.
62. He, T.; Puente Santiago, A.R.; Du, A. Atomically Embedded Asymmetrical Dual-Metal Dimers on N-Doped Graphene for Ultra-Efficient Nitrogen Reduction Reaction. *J. Catal.* **2020**, *388*, 77–83. https://doi.org/10.1016/j.jcat.2020.05.009.

63. Ling, C.; Zhang, Y.; Li, Q.; et al. New Mechanism for N_2 Reduction: The Essential Role of Surface Hydrogenation. *J. Am. Chem. Soc.* **2019**, *141*, 18264–18270. https://doi.org/10.1021/jacs.9b09232.
64. Siegbahn, P.E.M. The Mechanism for Nitrogenase Including All Steps. *Phys. Chem. Chem. Phys.* **2019**, *21*, 15747–15759. https://doi.org/10.1039/c9cp02073j.
65. Raugei, S.; Seefeldt, L.C.; Hoffman, B.M. Critical Computational Analysis Illuminates the Reductive-Elimination Mechanism That Activates Nitrogenase for N_2 Reduction. *Proc. Natl. Acad. Sci. USA* **2018**, *115*, E10521–E10530. https://doi.org/10.1073/pnas.1810211115.
66. Varley, J.B.; Wang, Y.; Chan, K.; et al. Mechanistic Insights into Nitrogen Fixation by Nitrogenase Enzymes. *Phys. Chem. Chem. Phys.* **2015**, *17*, 29541–29547. https://doi.org/10.1039/c5cp04034e.
67. Kim, M.-C.; Nam, H.; Choi, J.; et al. Hydrogen Bonding-Mediated Enhancement of Bioinspired Electrochemical Nitrogen Reduction on $Cu_{2-x}S$ Catalysts. *ACS Catal.* **2020**, *10*, 10577–10584. https://doi.org/10.1021/acscatal.0c01730.
68. Zhang, J.; Tian, X.; Liu, M.; et al. Cobalt-Modulated Molybdenum-Dinitrogen Interaction in MoS_2 for Catalyzing Ammonia Synthesis. *J. Am. Chem. Soc.* **2019**, *141*, 19269–19275. https://doi.org/10.1021/jacs.9b02501.
69. Mao, C.; Wang, J.; Zou, Y.; et al. Hydrogen Spillover to Oxygen Vacancy of $TiO_{2-x}H_y$/Fe: Breaking the Scaling Relationship of Ammonia Synthesis. *J. Am. Chem. Soc.* **2020**, *142*, 17403–17412. https://doi.org/10.1021/jacs.0c06118.
70. Marnellos, G.; Stoukides, M. Ammonia Synthesis at Atmospheric Pressure. *Science* **1998**, *282*, 98–100. https://doi.org/10.1126/science.282.5386.98.
71. Marnellos, G.; Zisekas, S.; Stoukides, M. Synthesis of Ammonia at Atmospheric Pressure with the Use of Solid State Proton Conductors. *J. Catal.* **2000**, *193*, 80–87. https://doi.org/10.1006/jcat.2000.2877.
72. Ouzounidou, M.; Skodra, A.; Kokkofitis, C.; et al. Catalytic and Electrocatalytic Synthesis of NH_3 in a H^+ Conducting Cell by Using an Industrial Fe Catalyst. *Solid State Ionics* **2007**, *178*, 153–159. https://doi.org/10.1016/j.ssi.2006.11.019.
73. Skodra, A.; Stoukides, M. Electrocatalytic Synthesis of Ammonia from Steam and Nitrogen at Atmospheric Pressure. *Solid State Ionics* **2009**, *180*, 1332–1336. https://doi.org/10.1016/j.ssi.2009.08.001.
74. Vasileiou, E.; Kyriakou, V.; Garagounis, I.; et al. Electrochemical Enhancement of Ammonia Synthesis in a $BaZr_{0.7}Ce_{0.2}Y_{0.1}O_{2.9}$ Solid Electrolyte Cell. *Solid State Ionics* **2016**, *288*, 357–362. https://doi.org/10.1016/j.ssi.2015.12.022.
75. Hirakawa, H.; Hashimoto, M.; Shiraishi, Y.; et al. Photocatalytic Conversion of Nitrogen to Ammonia with Water on Surface Oxygen Vacancies of Titanium Dioxide. *J. Am. Chem. Soc.* **2017**, *139*, 10929–10936. https://doi.org/10.1021/jacs.7b06634.
76. Xie, X.-Y.; Xiao, P.; Fang, W.-H.; et al. Probing Photocatalytic Nitrogen Reduction to Ammonia with Water on the Rutile TiO_2 (110) Surface by First-Principles Calculations. *ACS Catal.* **2019**, *9*, 9178–9187. https://doi.org/10.1021/acscatal.9b01551.
77. Kuang, M.; Wang, Y.; Fang, W.; et al. Efficient Nitrate Synthesis via Ambient Nitrogen Oxidation with Ru-Doped TiO_2/RuO_2 Electrocatalysts. *Adv. Mater.* **2020**, *32*, 2002189. https://doi.org/10.1002/adma.202002189.
78. Yuan, S.J.; Chen, J.J.; Lin, Z.Q.; et al. Nitrate Formation from Atmospheric Nitrogen and Oxygen Photocatalysed by Nano-Sized Titanium Dioxide. *Nat. Commun.* **2013**, *4*, 2249. https://doi.org/10.1038/ncomms3249.
79. Comer, B.M.; Medford, A.J. Analysis of Photocatalytic Nitrogen Fixation on Rutile TiO_2(110). *ACS Sustainable Chem. Eng.* **2018**, *6*, 4648–4660. https://doi.org/10.1021/acssuschemeng.7b03652.
80. Zhang, L.; Cong, M.; Ding, X.; et al. A Janus Fe-SnO_2 Catalyst That Enables Bifunctional Electrochemical Nitrogen Fixation. *Angew. Chem. Int. Ed.* **2020**, *59*, 10888–10893. https://doi.org/10.1002/anie.202003518.
81. Liu, Y.; Cheng, M.; He, Z.; et al. Pothole-Rich Ultrathin WO_3 Nanosheets that Trigger N≡N Bond Activation of Nitrogen for Direct Nitrate Photosynthesis. *Angew. Chem. Int. Ed.* **2019**, *58*, 731–735. https://doi.org/10.1002/anie.201808177.
82. Vasileff, A.; Xu, C.; Jiao, Y.; et al. Surface and Interface Engineering in Copper-Based Bimetallic Materials for Selective CO_2 Electroreduction. *Chem* **2018**, *4*, 1809–1831. https://doi.org/10.1016/j.chempr.2018.05.001.
83. Andersen, M.; Medford, A.J.; Nørskov, J.K.; et al. Scaling-Relation-Based Analysis of Bifunctional Catalysis: The Case for Homogeneous Bimetallic Alloys. *ACS Catal.* **2017**, *7*, 3960–3967. https://doi.org/10.1021/acscatal.7b00482.
84. Andersen, M.; Medford, A.J.; Nørskov, J.K.; et al. Analyzing the Case for Bifunctional Catalysis. *Angew. Chem. Int. Ed.* **2016**, *55*, 5210–5214. https://doi.org/10.1002/anie.201601049.
85. Shi, L.; Yin, Y.; Wang, S.; et al. Rational Catalyst Design for N_2 Reduction under Ambient Conditions: Strategies toward Enhanced Conversion Efficiency. *ACS Catal.* **2020**, *10*, 6870–6899. https://doi.org/10.1021/acscatal.0c01081.
86. Medford, A.J.; Vojvodic, A.; Hummelshøj, J.S.; et al. From the Sabatier Principle to a Predictive Theory of Transition-Metal Heterogeneous Catalysis. *J. Catal.* **2015**, *328*, 36–42. https://doi.org/10.1016/j.jcat.2014.12.033.
87. Vojvodic, A.; Nørskov, J.K. New Design Paradigm for Heterogeneous Catalysts. *Natl. Sci. Rev.* **2015**, *2*, 140–149. https://doi.org/10.1093/nsr/nwv023.

88. Suryanto, B.H.R.; Wang, D.; Azofra, L.M.; et al. MoS_2 Polymorphic Engineering Enhances Selectivity in the Electrochemical Reduction of Nitrogen to Ammonia. *ACS Energy Lett.* **2018**, *4*, 430–435. https://doi.org/10.1021/acsenergylett.8b02257.
89. Wang, J.; Yu, L.; Hu, L.; et al. Ambient Ammonia Synthesis via Palladium-Catalyzed Electrohydrogenation of Dinitrogen at Low Overpotential. *Nat. Commun.* **2018**, *9*, 1795. https://doi.org/10.1038/s41467-018-04213-9.
90. Lai, F.; Chen, N.; Ye, X.; et al. Refining Energy Levels in ReS_2 Nanosheets by Low-Valent Transition-Metal Doping for Dual-Boosted Electrochemical Ammonia/Hydrogen Production. *Adv. Funct. Mater.* **2020**, *30*, 1907376. https://doi.org/10.1002/adfm.201907376.
91. Li, J.; Yu, Y.; Jiang, S.P.; et al. Electronic Engineering of Spinels for Advanced Electrocatalysis. *Nanoscale Horiz.* **2026**, *11*, 357–374. https://doi.org/10.1039/D5NH00539F.
92. Xu, W.; Fan, G.; Chen, J.; et al. Nanoporous Palladium Hydride for Electrocatalytic N_2 Reduction under Ambient Conditions. *Angew. Chem. Int. Ed.* **2020**, *59*, 3511–3516. https://doi.org/10.1002/anie.201914335.
93. Fukui, K.; Iimura, S.; Tada, T.; et al. Characteristic Fast H^- Ion Conduction in Oxygen-Substituted Lanthanum Hydride. *Nat. Commun.* **2019**, *10*, 2578. https://doi.org/10.1038/s41467-019-10492-7.
94. Li, L.; Zhang, T.; Cai, J.; et al. Operando Spectroscopic and Isotopic-Label Directed Observation of LaN-Promoted Ru/ZrH_2 Catalyst for Ammonia Synthesis via Associative and Chemical Looping Route. *J. Catal.* **2020**, *389*, 218–228. https://doi.org/10.1016/j.jcat.2020.05.039.
95. Lu, F.; Yi, D.; Liu, S.; et al. Engineering Platinum-Oxygen Dual Catalytic Sites via Charge Transfer towards High-Efficient Hydrogen Evolution. *Angew. Chem. Int. Ed.* **2020**, *59*, 19460–19467. https://doi.org/10.1002/anie.202008117.
96. Wang, J.; Liu, W.; Luo, G.; et al. Synergistic Effect of Well-Defined Dual Sites Boosting the Oxygen Reduction Reaction. *Energy Environ. Sci.* **2018**, *11*, 3375–3379. https://doi.org/10.1039/c8ee02656d.
97. Chen, C.; Yan, X.; Liu, S.; et al. Highly Efficient Electroreduction of CO_2 to C_{2+} Alcohols on Heterogeneous Dual Active Sites. *Angew. Chem. Int. Ed.* **2020**, *59*, 16459–16464. https://doi.org/10.1002/anie.202006847.
98. Xiao, B.B.; Yang, L.; Yu, L.B.; et al. The VN_3 Embedded Graphane with the Improved Selectivity for Nitrogen Fixation. *Appl. Surf. Sci.* **2020**, *513*, 145855. https://doi.org/10.1016/j.apsusc.2020.145855.
99. Zeinalipour-Yazdi, C.D.; Hargreaves, J.S.J.; Catlow, C.R.A. DFT-D3 Study of Molecular N_2 and H_2 Activation on Co_3Mo_3N Surfaces. *J. Phys. Chem. C* **2016**, *120*, 21390–21398. https://doi.org/10.1021/acs.jpcc.6b04748.
100. Chen, Z.W.; Yan, J.M.; Jiang, Q. Single or Double: Which Is the Altar of Atomic Catalysts for Nitrogen Reduction Reaction? *Small Methods* **2018**, *3*, 1800291. https://doi.org/10.1002/smtd.201800291.
101. Wang, S.; Shi, L.; Bai, X.; et al. Highly Efficient Photo-/Electrocatalytic Reduction of Nitrogen into Ammonia by Dual-Metal Sites. *ACS Cent. Sci.* **2020**, *6*, 1762–1773. https://doi.org/10.1021/acscentsci.0c00552.
102. Jacobsen, C.J.H.; Dahl, S.; Clausen, B.S.; et al. Catalyst Design by Interpolation in the Periodic Table: Bimetallic Ammonia Synthesis Catalysts. *J. Am. Chem. Soc.* **2001**, *123*, 8404–8405. https://doi.org/10.1021/ja010963d.
103. Xue, Z.H.; Zhang, S.N.; Lin, Y.X.; et al. Electrochemical Reduction of N_2 into NH_3 by Donor-Acceptor Couples of Ni and Au Nanoparticles with a 67.8% Faradaic Efficiency. *J. Am. Chem. Soc.* **2019**, *141*, 14976–14980. https://doi.org/10.1021/jacs.9b07963.
104. Han, L.; Ren, Z.; Ou, P.; et al. Modulating Single-Atom Pd Sites with Cu for Enhanced Ambient Ammonia Electrosynthesis. *Angew. Chem. Int. Ed.* **2021**, *60*, 345–350. https://doi.org/10.1002/anie.202010159.
105. Liu, W.; Han, L.; Wang, H.-T.; et al. FeMo Sub-Nanoclusters/Single Atoms for Neutral Ammonia Electrosynthesis. *Nano Energy* **2020**, *77*, 105078. https://doi.org/10.1016/j.nanoen.2020.105078.
106. Wang, X.; Qiu, S.; Feng, J.; et al. Confined Fe-Cu Clusters as Sub-Nanometer Reactors for Efficiently Regulating the Electrochemical Nitrogen Reduction Reaction. *Adv. Mater.* **2020**, *32*, 2004382. https://doi.org/10.1002/adma.202004382.
107. Liu, Y.; Zhang, X.; Chen, Z.; et al. Electrocatalytic Reduction of Nitrogen on FeAg/Si for Ammonia Synthesis: A Simple Strategy for Continuous Regulation of Faradaic Efficiency by Controlling H^+ Ions Transfer Rate. *Appl. Catal. B* **2021**, *280*, 119606. https://doi.org/10.1016/j.apcatb.2020.119606.
108. Cromer, D.T.; Mills, R.L.; Schiferi, D.; et al. The Structure of N_2 at 49 Kbar and 299 K. *Acta Crystallogr. Sect. B Struct. Crystallogr. Cryst. Chem.* **1980**, *B37*, 8–11. https://doi.org/10.1107/S0567740881002070.
109. Mitchell, S.; Perez-Ramirez, J. Single Atom Catalysis: A Decade of Stunning Progress and the Promise for a Bright Future. *Nat. Commun.* **2020**, *11*, 4302. https://doi.org/10.1038/s41467-020-18182-5.
110. Guo, Y.; Yao, Z.; Zhan, S.; et al. Molybdenum and Boron Synergistically Boosting Efficient Electrochemical Nitrogen Fixation. *Nano Energy* **2020**, *78*, 105391. https://doi.org/10.1016/j.nanoen.2020.105391.
111. Dai, C.; Sun, Y.; Chen, G.; et al. Electrochemical Oxidation of Nitrogen towards Direct Nitrate Production on Spinel Oxides. *Angew. Chem. Int. Ed.* **2020**, *59*, 9418–9422. https://doi.org/10.1002/anie.202002923.
112. Han, S.; Wang, C.; Wang, Y.; et al. Electrosynthesis of Nitrate via the Oxidation of Nitrogen on Tensile Strained Palladium Porous Nanosheets. *Angew. Chem. Int. Ed.* **2021**, *60*, 4474–4478. https://doi.org/10.1002/anie.202014017.

113. Jia, H.P.; Quadrelli, E.A. Mechanistic Aspects of Dinitrogen Cleavage and Hydrogenation to Produce Ammonia in Catalysis and Organometallic Chemistry: Relevance of Metal Hydride Bonds and Dihydrogen. *Chem. Soc. Rev.* **2014**, *43*, 547–564. https://doi.org/10.1039/c3cs60206k.
114. Li, P.; Jin, Z.; Fang, Z.; et al. A Surface Strained and Geometry Tailored Nanoreactor Promotes the Ammonia Electrosynthesis. *Angew. Chem. Int. Ed.* **2020**, *59*, 22610–22616. https://doi.org/10.1002/anie.202011596.
115. Gevantman, L.H. Solubility of Selected Gases in Water. In *CRC Handbook of Chemistry and Physics*, 97th ed.; CRC Press: Boca Raton, FL, USA, 2016; pp. 5–134.
116. Li, X.; Sun, X.; Zhang, L.; et al. Efficient Photocatalytic Fixation of N_2 by KOH-Treated g-C_3N_4. *J. Mater. Chem. A* **2018**, *6*, 3005–3011. https://doi.org/10.1039/c7ta09762j.
117. Singh, A.R.; Rohr, B.A.; Schwalbe, J.A.; et al. Electrochemical Ammonia Synthesis—The Selectivity Challenge. *ACS Catal.* **2016**, *7*, 706–709. https://doi.org/10.1021/acscatal.6b03035.
118. Suryanto, B.H.R.; Kang, C.S.M.; Wang, D.; et al. Rational Electrode–Electrolyte Design for Efficient Ammonia Electrosynthesis under Ambient Conditions. *ACS Energy Lett.* **2018**, *3*, 1219–1224. https://doi.org/10.1021/acsenergylett.8b00487.
119. Tian, Y.; Liu, Y.; Wang, H.; et al. Electrocatalytic Reduction of Nitrogen to Ammonia in Ionic Liquids. *ACS Sustainable Chem. Eng.* **2022**, *10*, 4345–4358. https://doi.org/10.1021/acssuschemeng.2c00018.
120. Zhou, F.; Azofra, L.M.; Ali, M.; et al. Electro-Synthesis of Ammonia from Nitrogen at Ambient Temperature and Pressure in Ionic Liquids. *Energy Environ. Sci.* **2017**, *10*, 2516–2520. https://doi.org/10.1039/c7ee02716h.
121. Kang, C.S.M.; Zhang, X.; MacFarlane, D.R. High Nitrogen Gas Solubility and Physicochemical Properties of [C_4mpyr][eFAP]—Fluorinated Solvent Mixtures. *J. Phys. Chem. C* **2019**, *123*, 21376–21385. https://doi.org/10.1021/acs.jpcc.9b06000.
122. Ortuno, M.A.; Holloczki, O.; Kirchner, B.; et al. Selective Electrochemical Nitrogen Reduction Driven by Hydrogen Bond Interactions at Metal-Ionic Liquid Interfaces. *J. Phys. Chem. Lett.* **2019**, *10*, 513–517. https://doi.org/10.1021/acs.jpclett.8b03409.
123. Zou, H.; Rong, W.; Wei, S.; et al. Regulating Kinetics and Thermodynamics of Electrochemical Nitrogen Reduction with Metal Single-Atom Catalysts in a Pressurized Electrolyser. *Proc. Natl. Acad. Sci. USA* **2020**, *117*, 29462–29468. https://doi.org/10.1073/pnas.2015108117.
124. Cheng, H.; Cui, P.; Wang, F.; et al. High Efficiency Electrochemical Nitrogen Fixation Achieved with a Lower Pressure Reaction System by Changing the Chemical Equilibrium. *Angew. Chem. Int. Ed.* **2019**, *58*, 15541–15547. https://doi.org/10.1002/anie.201910658.
125. Zhang, S.; Duan, G.; Qiao, L.; et al. Electrochemical Ammonia Synthesis from N_2 and H_2O Catalyzed by Doped $LaFeO_3$ Perovskite under Mild Conditions. *Ind. Eng. Chem. Res.* **2019**, *58*, 14602–14607. https://doi.org/10.1021/acs.iecr.9b00833.
126. Qiao, L.; Duan, G.; Zhang, S.; et al. Electrochemical Ammonia Synthesis Catalyzed with a CoFe Layered Double Hydroxide—A New Initiative in Clean Fuel Synthesis. *J. Cleaner Prod.* **2020**, *250*, 119525. https://doi.org/10.1016/j.jclepro.2019.119525.
127. Ba, K.; Wang, G.K.; Ye, T.; et al. Single Faceted Two-Dimensional Mo_2C Electrocatalyst for Highly Efficient Nitrogen Fixation. *ACS Catal.* **2020**, *10*, 7864–7870. https://doi.org/10.1021/acscatal.0c01127.
128. Ji, S.G.; Kim, H.; Park, C.; et al. Underestimation of Platinum Electrocatalysis Induced by Carbon Monoxide Evolved from Graphite Counter Electrodes. *ACS Catal.* **2020**, *10*, 10773–10783. https://doi.org/10.1021/acscatal.0c01783.
129. Hanifpour, F.; Sveinbjornson, A.; Canales, C.P.; et al. Preparation of Nafion® Membranes for Reliable Ammonia Quantification in Nitrogen Reduction Reaction Experiments. *Angew. Chem. Int. Ed.* **2020**, *59*, 23138–23142. https://doi.org/10.1002/anie.202007998.
130. Liu, H.; Zhang, Y.; Luo, J. The Removal of Inevitable NO Species in Catalysts and the Selection of Appropriate Membrane for Measuring Electrocatalytic Ammonia Synthesis Accurately. *J. Energy Chem.* **2020**, *49*, 51–58. https://doi.org/10.1016/j.jechem.2020.01.029.
131. Wang, H.; Chen, Y.; Fan, R.; et al. Selective Electrochemical Reduction of Nitrogen to Ammonia by Adjusting the Three-Phase Interface. *Research* **2019**, *2019*, 1401209. https://doi.org/10.34133/2019/1401209.
132. Weekes, D.M.; Salvatore, D.A.; Reyes, A.; et al. Electrolytic CO_2 Reduction in a Flow Cell. *Acc. Chem. Res.* **2018**, *51*, 910–918. https://doi.org/10.1021/acs.accounts.8b00010.
133. Li, J.; Chen, S.; Quan, F.; et al. Accelerated Dinitrogen Electroreduction to Ammonia via Interfacial Polarization Triggered by Single-Atom Protrusions. *Chem* **2020**, *6*, 885–901. https://doi.org/10.1016/j.chempr.2020.01.013.
134. Chen, S.; Perathoner, S.; Ampelli, C.; et al. Electrocatalytic Synthesis of Ammonia at Room Temperature and Atmospheric Pressure from Water and Nitrogen on a Carbon-Nanotube-Based Electrocatalyst. *Angew. Chem. Int. Ed.* **2017**, *56*, 2699–2703. https://doi.org/10.1002/anie.201609533.

135. Chen, S.; Perathoner, S.; Ampelli, C.; et al. Room-Temperature Electrocatalytic Synthesis of NH_3 from H_2O and N_2 in a Gas–Liquid–Solid Three-Phase Reactor. *ACS Sustain. Chem. Eng.* **2017**, *5*, 7393–7400. https://doi.org/10.1021/acssuschemeng.7b01742.
136. Chen, S.; Perathoner, S.; Ampelli, C.; et al. Enhanced Performance in the Direct Electrocatalytic Synthesis of Ammonia from N_2 and H_2O by an *In-Situ* Electrochemical Activation of CNT-Supported Iron Oxide Nanoparticles. *J. Energy Chem.* **2020**, *49*, 22–32. https://doi.org/10.1016/j.jechem.2020.01.011.
137. Chen, S.; Perathoner, S.; Ampelli, C.; et al. Direct Synthesis of Ammonia from N_2 and H_2O on Different Iron Species Supported on Carbon Nanotubes Using a Gas-Phase Electrocatalytic Flow Reactor. *ChemElectroChem* **2020**, *7*, 3028–3037. https://doi.org/10.1002/celc.202000514.
138. Cui, X.; Tang, C.; Liu, X.M.; et al. Highly Selective Electrochemical Reduction of Dinitrogen to Ammonia at Ambient Temperature and Pressure over Iron Oxide Catalysts. *Chem. Eur. J.* **2018**, *24*, 18494–18501. https://doi.org/10.1002/chem.201800535.
139. Wei, X.; Vogel, D.; Keller, L.; et al. Microtubular Gas Diffusion Electrode Based on Ruthenium-Carbon Nanotubes for Ambient Electrochemical Nitrogen Reduction to Ammonia. *ChemElectroChem* **2020**, *7*, 4679–4684. https://doi.org/10.1002/celc.202001370.
140. Liu, Y.; Huang, B.; Chen, X.; et al. Electrocatalytic Production of Ammonia: Biomimetic Electrode–Electrolyte Design for Efficient Electrocatalytic Nitrogen Fixation under Ambient Conditions. *Appl. Catal. B* **2020**, *271*, 118919. https://doi.org/10.1016/j.apcatb.2020.118919.
141. Salvatore, D.; Berlinguette, C.P. Voltage Matters When Reducing CO_2 in an Electrochemical Flow Cell. *ACS Energy Lett.* **2019**, *5*, 215–220. https://doi.org/10.1021/acsenergylett.9b02356.
142. Zhang, Z.; Melo, L.; Jansonius, R.P.; et al. pH Matters When Reducing CO_2 in an Electrochemical Flow Cell. *ACS Energy Lett.* **2020**, *5*, 3101–3107. https://doi.org/10.1021/acsenergylett.0c01606.
143. Kani, N.C.; Prajapati, A.; Collins, B.A.; et al. Competing Effects of pH, Cation Identity, H_2O Saturation, and N_2 Concentration on the Activity and Selectivity of Electrochemical Reduction of N_2 to NH_3 on Electrodeposited Cu at Ambient Conditions. *ACS Catal.* **2020**, *10*, 14592–14603. https://doi.org/10.1021/acscatal.0c04864.
144. Back, S.; Jung, Y. On the Mechanism of Electrochemical Ammonia Synthesis on the Ru Catalyst. *Phys. Chem. Chem. Phys.* **2016**, *18*, 9161–9166. https://doi.org/10.1039/c5cp07363d.
145. Li, Q.; Qiu, S.; He, L.; et al. Impact of H-Termination on the Nitrogen Reduction Reaction of Molybdenum Carbide as an Electrochemical Catalyst. *Phys. Chem. Chem. Phys.* **2018**, *20*, 23338–23343. https://doi.org/10.1039/c8cp04474k.
146. Zheng, J.; Lyu, Y.; Qiao, M.; et al. Photoelectrochemical Synthesis of Ammonia on the Aerophilic-Hydrophilic Heterostructure with 37.8% Efficiency. *Chem* **2019**, *5*, 617–633. https://doi.org/10.1016/j.chempr.2018.12.003.
147. Guan, R.; Wang, D.; Zhang, Y.; et al. Enhanced Photocatalytic N_2 Fixation via Defective and Fluoride Modified TiO_2 Surface. *Appl. Catal. B* **2021**, *282*, 119580. https://doi.org/10.1016/j.apcatb.2020.119580.
148. Sun, Y.; Jiang, T.; Duan, J.; et al. Two-Dimensional Nanomesh Arrays as Bifunctional Catalysts for N_2 Electrolysis. *ACS Catal.* **2020**, *10*, 11371–11379. https://doi.org/10.1021/acscatal.0c02745.
149. Qin, M.; Li, X.; Gan, G.; et al. Boosting Electrocatalytic Nitrogen Fixation with Co–N_3 Site-Decorated Porous Carbon. *ACS Sustainable Chem. Eng.* **2020**, *8*, 13430–13439. https://doi.org/10.1021/acssuschemeng.0c04021.
150. Wang, H.; Wang, L.; Wang, Q.; et al. Ambient Electrosynthesis of Ammonia: Electrode Porosity and Composition Engineering. *Angew. Chem. Int. Ed.* **2018**, *57*, 12360–12364. https://doi.org/10.1002/anie.201805514.
151. Li, H.; Shang, J.; Ai, Z.; et al. Efficient Visible Light Nitrogen Fixation with BiOBr Nanosheets of Oxygen Vacancies on the Exposed {001} Facets. *J. Am. Chem. Soc.* **2015**, *137*, 6393–6399. https://doi.org/10.1021/jacs.5b03105.
152. Ma, X.; Liu, Z.; Sun, H.; et al. Cu(N_2)-Li Battery for Ammonia Synthesis. *J. Phys. Chem. Lett.* **2024**, *15*, 6435–6442. https://doi.org/10.1021/acs.jpclett.4c01328.
153. Ma, X.; Li, J.; Zhou, H.; et al. Li-N_2 Battery for Ammonia Synthesis and Computational Insight. *ACS Appl. Mater. Interfaces* **2023**, *15*, 19032–19042. https://doi.org/10.1021/acsami.3c01929.
154. Ma, X.; Li, J.; Zhou, H.; et al. Continuous Ammonia Synthesis Using Ru Nanoparticles Based on Li-N_2 Battery. *Mater. Today Energy* **2022**, *29*, 101113–101122. https://doi.org/10.1016/j.mtener.2022.101113.
155. Ma, X.; Sun, H.; Li, J.; et al. "Continuous" Nitrogen Reduction Synthesis of Ammonia Based on Li-N_2 Battery System. *Acta Chim. Sinica* **2022**, *80*, 861–866. https://doi.org/10.6023/A22020088.
156. Ma, X.; Ma, Y.; Sun, H.; et al. Cycle Issue and Failure Analysis of Li–N_2 Batteries. *ACS Sustain. Chem. Eng.* **2025**, *13*, 2521–2528. https://doi.org/10.1021/acssuschemeng.4c09349.
157. Mangini, A.; Garbujo, A.; Biasi, P.; et al. Debunking Pitfalls of Li–N_2 Cells for Ammonia Electroproduction: Is This Setup Affordable to Prove Nitro-Fixation before Lithium Plating? *ACS Electrochem.* **2025**, *1*, 2866–2877. https://doi.org/10.1021/acselectrochem.5c00402.
158. Liu, C.; Li, Q.; Wu, C.; et al. Single-Boron Catalysts for Nitrogen Reduction Reaction. *J. Am. Chem. Soc.* **2019**, *141*, 2884–2888. https://doi.org/10.1021/jacs.8b13165.

159. Ling, C.; Niu, X.; Li, Q.; et al. Metal-Free Single Atom Catalyst for N_2 Fixation Driven by Visible Light. *J. Am. Chem. Soc.* **2018**, *140*, 14161–14168. https://doi.org/10.1021/jacs.8b07472.
160. Hao, Q.; Liu, C.; Jia, G.; et al. Catalytic Reduction of Nitrogen to Produce Ammonia by Bismuth-Based Catalysts: State of the Art and Future Prospects. *Mater. Horiz.* **2020**, *7*, 1014–1029. https://doi.org/10.1039/c9mh01668f.
161. Choi, J.; Du, H.-L.; Nguyen, C.K.; et al. Electroreduction of Nitrates, Nitrites, and Gaseous Nitrogen Oxides: A Potential Source of Ammonia in Dinitrogen Reduction Studies. *ACS Energy Lett.* **2020**, *5*, 2095–2097. https://doi.org/10.1021/acsenergylett.0c00924.
162. MacFarlane, D.; Simonov, A.; Suryanto, B.H.R.; et al. Promoting Nitrogen Electroreduction to Ammonia with Bismuth Nanocrystals and Potassium Cations in Water. *ChemRxiv* **2020**. https://doi.org/10.26434/chemrxiv.11768814.v1.
163. Mao, C.; Wang, J.; Zou, Y.; et al. Anion (O, N, C, and S) Vacancies Promoted Photocatalytic Nitrogen Fixation. *Green Chem.* **2019**, *21*, 2852–2867. https://doi.org/10.1039/c9gc01010f.
164. Liu, Y.; Kong, X.; Guo, X.; et al. Enhanced N_2 Electroreduction over $LaCoO_3$ by Introducing Oxygen Vacancies. *ACS Catal.* **2019**, *10*, 1077–1085. https://doi.org/10.1021/acscatal.9b03864.
165. Yang, X.; Ling, F.; Su, J.; et al. Insights into the Role of Cation Vacancy for Significantly Enhanced Electrochemical Nitrogen Reduction. *Appl. Catal. B* **2020**, *264*, 118477. https://doi.org/10.1016/j.apcatb.2019.118477.
166. Peng, W.; Luo, M.; Xu, X.; et al. Spontaneous Atomic Ruthenium Doping in Mo_2CTX MXene Defects Enhances Electrocatalytic Activity for the Nitrogen Reduction Reaction. *Adv. Energy Mater.* **2020**, *10*, 2001364. https://doi.org/10.1002/aenm.202001364.
167. Yao, D.; Tang, C.; Li, L.; et al. *In Situ* Fragmented Bismuth Nanoparticles for Electrocatalytic Nitrogen Reduction. *Adv. Energy Mater.* **2020**, *10*, 2001289. https://doi.org/10.1002/aenm.202001289.
168. Liu, S.; Wang, M.; Qian, T.; et al. Facilitating Nitrogen Accessibility to Boron-Rich Covalent Organic Frameworks via Electrochemical Excitation for Efficient Nitrogen Fixation. *Nat. Commun.* **2019**, *10*, 3898. https://doi.org/10.1038/s41467-019-11846-x.
169. Manjunatha, R.; Schechter, A. Electrochemical Synthesis of Ammonia Using Ruthenium–Platinum Alloy at Ambient Pressure and Low Temperature. *Electrochem. Commun.* **2018**, *90*, 96–100. https://doi.org/10.1016/j.elecom.2018.04.008.
170. de Araujo, R.G.; Perez, J. Nitrogen Electrochemical Reduction Reaction Pathways Evidenced by Online Electrochemical Mass Spectrometry and Isotope Labeling on the MoS_2 Surface. *ACS Electrochem.* **2025**, *1*, 294–302. https://doi.org/10.1021/acselectrochem.4c00135.
171. Yao, Y.; Wang, H.; Yuan, X.-Z.; et al. Electrochemical Nitrogen Reduction Reaction on Ruthenium. *ACS Energy Lett.* **2019**, *4*, 1336–1341. https://doi.org/10.1021/acsenergylett.9b00699.
172. Yao, Y.; Zhu, S.; Wang, H.; et al. A Spectroscopic Study on the Nitrogen Electrochemical Reduction Reaction on Gold and Platinum Surfaces. *J. Am. Chem. Soc.* **2018**, *140*, 1496–1501. https://doi.org/10.1021/jacs.7b12101.
173. Yao, Y.; Zhu, S.; Wang, H.; et al. A Spectroscopic Study of Electrochemical Nitrogen and Nitrate Reduction on Rhodium Surfaces. *Angew. Chem. Int. Ed.* **2020**, *59*, 10479–10483. https://doi.org/10.1002/anie.202003071.
174. Qu, X.; Shen, L.; Mao, Y.; et al. Facile Preparation of Carbon Shells-Coated O-Doped Molybdenum Carbide Nanoparticles as High Selective Electrocatalysts for Nitrogen Reduction Reaction under Ambient Conditions. *ACS Appl. Mater. Interfaces* **2019**, *11*, 31869–31877. https://doi.org/10.1021/acsami.9b09007.
175. Yang, X.; Nash, J.; Anibal, J.; et al. Mechanistic Insights into Electrochemical Nitrogen Reduction Reaction on Vanadium Nitride Nanoparticles. *J. Am. Chem. Soc.* **2018**, *140*, 13387–13391. https://doi.org/10.1021/jacs.8b08379.
176. Luo, S.; Li, X.; Wang, M.; et al. Long-Term Electrocatalytic N_2 Fixation by MOF-Derived Y-Stabilized ZrO_2: Insight into the Deactivation Mechanism. *J. Mater. Chem. A* **2020**, *8*, 5647–5654. https://doi.org/10.1039/d0ta01154a.
177. Chen, G.F.; Ren, S.; Zhang, L.; et al. Advances in Electrocatalytic N_2 Reduction-Strategies to Tackle the Selectivity Challenge. *Small Methods* **2018**, *3*, 1800337–1800357. https://doi.org/10.1002/smtd.201800337.
178. Singh, A.R.; Rohr, B.A.; Statt, M.J.; et al. Strategies toward Selective Electrochemical Ammonia Synthesis. *ACS Catal.* **2019**, *9*, 8316–8324. https://doi.org/10.1021/acscatal.9b02245.
179. Su, H.; Chen, L.; Chen, Y.; et al. Single Atoms of Iron on MoS_2 Nanosheets for N_2 Electroreduction into Ammonia. *Angew. Chem. Int. Ed.* **2020**, *59*, 20411–20416. https://doi.org/10.1002/anie.202009217.
180. Sim, H.Y.F.; Chen, J.R.T.; Koh, C.S.L.; et al. ZIF-Induced d-Band Modification in a Bimetallic Nanocatalyst: Achieving Over 44% Efficiency in the Ambient Nitrogen Reduction Reaction. *Angew. Chem. Int. Ed.* **2020**, *59*, 16997–17003. https://doi.org/10.1002/anie.202006071.
181. Mukherjee, S.; Yang, X.; Shan, W.; et al. Atomically Dispersed Single Ni Site Catalysts for Nitrogen Reduction toward Electrochemical Ammonia Synthesis Using N_2 and H_2O. *Small Methods* **2020**, *4*, 1900821. https://doi.org/10.1002/smtd.201900821.
182. Zhao, H.; Zhang, D.; Li, H.; et al. Exposure of Definite Palladium Facets Boosts Electrocatalytic Nitrogen Fixation at Low Overpotential. *Adv. Energy Mater.* **2020**, *10*, 2002131. https://doi.org/10.1002/aenm.202002131.

183. Bohra, D.; Chaudhry, J.H.; Burdyny, T.; et al. Modeling the Electrical Double Layer to Understand the Reaction Environment in a CO_2 Electrocatalytic System. *Energy Environ. Sci.* **2019**, *12*, 3380–3389. https://doi.org/10.1039/c9ee02485a.
184. Xue, S.; Garlyyev, B.; Watzele, S.; et al. Influence of Alkali Metal Cations on the Hydrogen Evolution Reaction Activity of Pt, Ir, Au, and Ag Electrodes in Alkaline Electrolytes. *ChemElectroChem* **2018**, *5*, 2326–2329. https://doi.org/10.1002/celc.201800690.
185. Guha, A.; Narayanaru, S.; Narayanan, T.N. Tuning the Hydrogen Evolution Reaction on Metals by Lithium Salt. *ACS Appl. Energy Mater.* **2018**, *1*, 7116–7122. https://doi.org/10.1021/acsaem.8b01546.
186. Perini, N.; Ticianelli, E.A. Oxygen Evolution on Gold: The Effects of Alkali-Metal Cations and Iron Impurities from Alkaline Electrolytes. *J. Catal.* **2019**, *378*, 277–282. https://doi.org/10.1016/j.jcat.2019.09.003.
187. Garcia, A.C.; Touzalin, T.; Nieuwland, C.; et al. Enhancement of Oxygen Evolution Activity of Nickel Oxyhydroxide by Electrolyte Alkali Cations. *Angew. Chem. Int. Ed.* **2019**, *58*, 12999–13003. https://doi.org/10.1002/anie.201905501.
188. Guha, A.; Narayanaru, S.; Kaley, N.M.; et al. Mechanistic Insight into High Yield Electrochemical Nitrogen Reduction to Ammonia Using Lithium Ions. *Mater. Today Commun.* **2019**, *21*, 100700. https://doi.org/10.1016/j.mtcomm.2019.100700.
189. Liu, K.W.; Ma, Y.B.; Guo, Y.; et al. Functional Binder with Enhanced Chemical Adsorption for Black Phosphorus Anode in Lithium-Ion Capacitors. *Adv. Funct. Mater.* **2024**, *34*, 2410451. https://doi.org/10.1002/adfm.202410451.
190. Hao, Y.-C.; Guo, Y.; Chen, L.-W.; et al. Promoting Nitrogen Electroreduction to Ammonia with Bismuth Nanocrystals and Potassium Cations in Water. *Nat. Catal.* **2019**, *2*, 448–456. https://doi.org/10.1038/s41929-019-0241-7.
191. Song, Y.; Johnson, D.; Peng, R.; et al. A Physical Catalyst for the Electrolysis of Nitrogen to Ammonia. *Sci. Adv.* **2018**, *4*, e1700336. https://doi.org/10.1126/sciadv.1700336.
192. Lindley, B.M.; Appel, A.M.; Krogh-Jespersen, K.; et al. Evaluating the Thermodynamics of Electrocatalytic N_2 Reduction in Acetonitrile. *ACS Energy Lett.* **2016**, *1*, 698–704. https://doi.org/10.1021/acsenergylett.6b00319.
193. Zhang, L.; Sharada, S.M.; Singh, A.R.; et al. A Theoretical Study of the Effect of a Non-Aqueous Proton Donor on Electrochemical Ammonia Synthesis. *Phys. Chem. Chem. Phys.* **2018**, *20*, 4982–4989. https://doi.org/10.1039/c7cp05484j.
194. Kim, K.; Lee, N.; Yoo, C.-Y.; et al. Communication—Electrochemical Reduction of Nitrogen to Ammonia in 2-Propanol under Ambient Temperature and Pressure. *J. Electrochem. Soc.* **2016**, *163*, F610–F612. https://doi.org/10.1149/2.0231607jes.
195. Köleli, F.; Röpke, T. Electrochemical Hydrogenation of Dinitrogen to Ammonia on a Polyaniline Electrode. *Appl. Catal. B* **2006**, *62*, 306–310. https://doi.org/10.1016/j.apcatb.2005.08.006.
196. Kim, K.; Yoo, C.-Y.; Kim, J.-N.; et al. Electrochemical Synthesis of Ammonia from Water and Nitrogen in Ethylenediamine under Ambient Temperature and Pressure. *J. Electrochem. Soc.* **2016**, *163*, F1523–F1526. https://doi.org/10.1149/2.0741614jes.
197. Sheets, B.L.; Botte, G.G. Electrochemical Nitrogen Reduction to Ammonia under Mild Conditions Enabled by a Polymer Gel Electrolyte. *Chem. Commun.* **2018**, *54*, 4250–4253. https://doi.org/10.1039/C8CC00657A.
198. Koh, C.S.L.; Lee, H.K.; Sim, H.Y.F.; et al. Turning Water from a Hindrance to the Promotor of Preferential Electrochemical Nitrogen Reduction. *Chem. Mater.* **2020**, *32*, 1674–1683. https://doi.org/10.1021/acs.chemmater.9b05313.
199. Lee, H.K.; Koh, C.S.L.; Lee, Y.H.; et al. Favoring the Unfavored: Selective Electrochemical Nitrogen Fixation Using a Reticular Chemistry Approach. *Sci. Adv.* **2018**, *4*, eaar3208. https://doi.org/10.1126/sciadv.aar3208.
200. Yang, Y.; Wang, S.Q.; Wen, H.; et al. Nanoporous Gold Embedded ZIF Composite for Enhanced Electrochemical Nitrogen Fixation. *Angew. Chem. Int. Ed.* **2019**, *58*, 15362–15366. https://doi.org/10.1002/anie.201909770.
201. Du, C.; Gao, Y.; Wang, J.; et al. Achieving 59% Faradaic Efficiency of the N_2 Electroreduction Reaction in an Aqueous Zn-N_2 Battery by Facilely Regulating the Surface Mass Transport on Metallic Copper. *Chem. Commun.* **2019**, *55*, 12801–12804. https://doi.org/10.1039/c9cc05978d.
202. Chen, Y.; Liu, H.; Ha, N.; et al. Revealing Nitrogen-Containing Species in Commercial Catalysts Used for Ammonia Electrosynthesis. *Nat. Catal.* **2020**, *3*, 1055–1061. https://doi.org/10.1038/s41929-020-00527-4.
203. Andersen, S.Z.; Čolić, V.; Yang, S.; et al. A Rigorous Electrochemical Ammonia Synthesis Protocol with Quantitative Isotope Measurements. *Nature* **2019**, *570*, 504–508. https://doi.org/10.1038/s41586-019-1260-x.
204. Choi, J.; Suryanto, B.H.R.; Wang, D.; et al. Identification and Elimination of False Positives in Electrochemical Nitrogen Reduction Studies. *Nat. Commun.* **2020**, *11*, 5546–5556. https://doi.org/10.1038/s41467-020-19130-z.
205. Dahl, S.; Logadottir, A.; Jacobsen, C.J.H.; et al. Electronic Factors in Catalysis: The Volcano Curve and the Effect of Promotion in Catalytic Ammonia Synthesis. *Appl. Catal. A* **2001**, *222*, 19–29. https://doi.org/10.1016/S0926-860X(01)00826-2.
206. Kibsgaard, J.; Nørskov, J.K.; Chorkendorff, I. The Difficulty of Proving Electrochemical Ammonia Synthesis. *ACS Energy Lett.* **2019**, *4*, 2986–2988. https://doi.org/10.1021/acsenergylett.9b02286.

207. Medford, A.J.; Hatzell, M.C. Photon-Driven Nitrogen Fixation: Current Progress, Thermodynamic Considerations, and Future Outlook. *ACS Catal.* **2017**, *7*, 2624–2643. https://doi.org/10.1021/acscatal.7b00439.
208. Rouwenhorst, K.H.R.; Engelmann, Y.; van 't Veer, K.; et al. Plasma-Driven Catalysis: Green Ammonia Synthesis with Intermittent Electricity. *Green Chem.* **2020**, *22*, 6258–6287. https://doi.org/10.1039/d0gc02058c.
209. NIST-JANAF Thermochemical Tables. Available online: https://janaf.nist.gov/ (accessed on 20 March 2025).